University of California

Los Angeles

# Computational Techniques to Ensure Valid Simulations of Brain Aneurysm Blood Flow

A thesis submitted in partial satisfaction

of the requirements for the degree

Master of Science in Computer Science

by

**Simon D. Shpilfoygel**

1997

© Copyright by

Simon D. Shpilfoygel

1997

The thesis of Simon D. Shpilfoygel is approved.

Alfonso F. Cardenas

Jack W. Carlyle

Daniel J. Valentino

Walter J. Karplus, Committee Chair

University of California, Los Angeles

1997

# Table of Contents


**1 Introduction . . . . . 1**

1.1 Importance of the Project . . . . . 2

1.1.1 Intracranial Aneurysms . . . . . 2

1.1.2 Causes . . . . . 7

1.1.3 Symptoms and Detection . . . . . 8

1.1.4 Treatment . . . . . 10

1.2 Digital Radiology . . . . . 14

1.3 Scope of Investigation . . . . . 15

1.4 Organization . . . . . 17

**2 Brain Aneurysm Blood Flow . . . . . 18**

2.1 Previous Studies . . . . . 18

2.2 Mathematical Model . . . . . 22

2.2.1 Assumptions . . . . . 22

2.2.2 Formulation of Characterizing Partial Differential Equations 26

2.2.3 Blood Properties . . . . . 29

2.3 Numerical Methods . . . . . 30

2.3.1 Survey of Numerical Methods . . . . . 30

2.3.2 Numerical Method Selection . . . . . 34

2.4 Simulation Software . . . . . 34

2.4.1 The Initial Selection . . . . . 34

2.4.2 Subsequent Changes . . . . . 35

**3 Brain Aneurysm Models . . . . . 38**

3.1 Model Constraints . . . . . 38

3.1.1 Size of Object Features . . . . . 38

3.1.2 Flow Velocity Constraints . . . . . 39

3.2 Sources of Geometry Data . . . . . 39

3.2.1 Visual observations and measurements . . . . . 39

3.2.2 Digital Subtraction Angiography . . . . . 40

3.2.3 Magnetic Resonance Imaging and Angiography . . . . . 43

3.2.4 Computed Tomography . . . . . 46

3.2.5 Conclusions . . . . . 46

3.3 Measurement of Arterial Blood Flow . . . . . 48

3.3.1 Electromagnetic Flow Meters . . . . . 49

3.3.2 Ultrasonic Flow Meters . . . . . 49

3.3.3 Videodensitometric Techniques . . . . . 52

3.3.4 Conclusions . . . . . 61

3.4 Geometric Modeling . . . . . 62

3.4.1 Requirements Imposed on Geometric Models by $NEKTON$ 63

3.4.2 Requirements Imposed on Geometric Models by $Fluent/UNS$ 64

3.4.3 Numerical Measures of Tetrahedral Grid Quality . . . . . 66

3.5 Physiologic Modeling . . . . . 68

3.5.1 Requirements Imposed by CFD Packages . . . . . 69

3.5.2 Requirements Imposed by the Validation Procedure . . . . 69

**4 Image Processing . . . . . 70**

4.1 Introduction . . . . . 70

4.2 Image Enhancement Techniques . . . . . 71

4.3 Segmentation Techniques . . . . . 72

4.3.1 Basic Segmentation Methods . . . . . 73

4.3.2 Advanced Segmentation Methods . . . . . 74

4.4 Off-the-shelf image processing software . . . . . 75

4.5 Selection of Image Processing Methods and Software . . . . . 76

4.5.1 Image Enhancement . . . . . 76

4.5.2 Segmentation . . . . . 76

4.5.3 Software . . . . . 77

**5 Validation . . . . . 78**

5.1 Previous Studies . . . . . 78

5.2 Validation Procedure . . . . . 79

5.2.1 Simulation Goals . . . . . 80

5.2.2 Available Experimental Results . . . . . 80

5.2.3 Simulation Results . . . . . 81

5.2.4 Procedure Selection . . . . . 81

5.3 Modeling Procedures . . . . . 82

5.3.1 Manual Geometric Modeling Procedure . . . . . 82
5.3.2 Automated Geometric Modeling Procedure . . . . . 83
5.3.3 Physiologic Modeling Procedure . . . . . 84
5.4 Models Used . . . . . 85
5.4.1 Physical System . . . . . 85
5.4.2 *In Vivo* Models . . . . . 85
5.4.3 Geometric Models . . . . . 86
5.4.4 Physiologic Models . . . . . 89
5.5 Analysis of Simulation Results . . . . . 96
5.5.1 Qualitative Analysis . . . . . 96
5.5.2 Quantitative Analysis . . . . . 102

**6 Conclusion . . . . . 111**
6.1 Overview . . . . . 111
6.2 Discussion . . . . . 112
6.3 Contributions . . . . . 115
6.4 Suggestions for Further Research . . . . . 115

**References . . . . . 117**

# List of Figures


1.1 A saccular aneurysm. . . . . 3

1.2 Schematic of circle of Willis with major arteries designated. . . . . 3

1.3 A ruptured aneurysm. . . . . 4

1.4 Schematic of bifurcation aneurysm with anatomic terms. . . . . 5

1.5 Schematic of lateral wall aneurysm with anatomic terms. . . . . 6

1.6 A fusiform aneurysm. . . . . 7

1.7 Vessel in vasospasm . . . . . 9

1.8 Path of microcatheter for endovascular brain aneurysm treatment. 12

1.9 Occlusion of an intracranial aneurysm with platinum coil. . . . . 13

1.10 UCLA PACS Architecture. . . . . 15

3.1 A typical sequence of angiographic images of a swine aneurysm, lateral projection. . . . . 41

3.2 Subtracted lateral angiographic projection of swine aneurysm. . . 42

3.3 Diagram of the *Cardiometrics* Doppler guide wire. . . . . 50

3.4 Doppler probe and angles of incidence. . . . . 51

3.5 An example of intravascular Doppler measurements. . . . . 52

3.6 An example of time–density curves for two ROIs. . . . . 54

3.7 Time–density curves. Time of peak amplitude. . . . . 55

3.8 Time–density curves. Time of half–peak amplitude. . . . . 55

3.9 Time-density curves. Time of peak gradient. . . . . 56

5.1 An anterioposterior projection of an aneurysm model. . . . . 87

5.2 A lateral projection of an aneurysm model. . . . . 87

5.3 A typical slice of a hexahedral mesh. A cross–section of the vessel is in the bottom and the aneurysm is in the top. . . . . 88

5.4 A typical slice of a hexahedral mesh. The aneurysm is atop an artery, the neck can be seen in the middle. . . . . 89

5.5 A geometric model of an aneurysm constructed in swine 895. . . . 90

5.6 Lateral angiogram of swine 193 with probe in the vessel segment directly below the aneurysmal neck. . . . . 92

5.7 Lateral angiogram of swine 895 with probe in the neck, measuring flow into the aneurysm. . . . . 92

5.8 Lateral angiogram of swine 895 with probe inserted inside the aneurysm through the vessel. . . . . 93

5.9 Lateral angiogram of swine 193 with probe inserted inside the aneurysm through the top of the aneurysm. . . . . 93

5.10 Lateral angiogram of swine 193 with probe located in the neck near its proximal lip facing out of the aneurysm (looped around the wall of the aneurysm). . . . . 94

5.11 Anteroposterior angiogram of swine 895 with probe inserted inside the aneurysm through the vessel. . . . . 94

5.12 Blood recirculation inside aneurysm, swine 895. . . . . 96

5.13 Blood recirculation inside aneurysm, swine 193. A vortex is near the distal lip, stagnant blood in the upper part of the fundus. . . 97

5.14 Blood recirculation inside an aneurysm, swine 687, time 0.075 $s$. . 98

5.15 Blood recirculation inside an aneurysm, swine 687, time 0.15 $s$. . . 99

5.16 Blood recirculation inside an aneurysm, swine 687, time 0.45 $s$. . . 99

5.17 Blood recirculation inside an aneurysm, swine 687, time 0.9 $s$. . . 100

5.18 Blood recirculation inside an aneurysm, swine 687, time 1.125 $s$. . 100

5.19 Blood recirculation inside aneurysm, swine 66, time 1.05 $s$. . . . . 101

5.20 Different Doppler probe positions inside the aneurysm and the parent vessel (sampling volumes not to scale). . . . . 102

5.21 Doppler strip chart of swine 895 with probe in position 7. . . . . 103

5.22 Numerical and experimental blood flow speed in swine 895 with Doppler probe in position 7. . . . . 104

5.23 Doppler strip chart of swine 895 with probe in position 4. . . . . 104

5.24 Numerical and experimental blood flow speed in swine 895 with Doppler probe in position 4. . . . . 105

5.25 Doppler strip chart of swine 895 with probe in position 5. . . . . 105

5.26 Numerical and experimental blood flow speed in swine 895 with Doppler probe in position 5. . . . . 106

5.27 Doppler strip chart of swine 895 with probe in position 4. . . . . 107

5.28 Blood flow speed in swine 895. The Doppler probe is in position 4, the numerical flow was measured in three points close to the tip of the probe. . . . . 107

5.29 Doppler strip chart of swine 895 with probe in position 2. . . . . 108

5.30 Blood flow speed in swine 895. The Doppler probe is in position 2, the numerical flow was measured in three points close to the tip of the probe. . . . . 108

# Acknowledgments

I owe many thanks:

To my advisor Prof. Walter Karplus for guidance, wisdom and patience.

To my research advisor, Prof. Daniel Valentino for continued support, inspiration and ideas.

To the members of the committee, Dr. Jack Carlyle and Dr. Alfonso Cardenas for reviewing this thesis.

To Prof. Gary Duckwiler and Prof. Suzie El–Saden for their interest in this work and helpful discussions.

To Dr. Michael Harreld for everything mentioned above and then some.

To RIS/PACS Operations and Development Teams in the Department of Radiological Sciences, UCLA School of Medicine for making the computers work long enough for me to finish this thesis.

To General Electric, Sun Microsystems and NIH for provided support.

To Target Therapeutics for the aneurysm pictures and Michael R. Harreld for the schematic of the Circle of Willis.

This research was supported in part by the NASA/Dryden Research Center under Grant FSC 2-374.

Abstract of the Thesis

# Computational Techniques to Ensure Valid Simulations of Brain Aneurysm Blood Flow

by

**Simon D. Shpilfoygel**

Master of Science in Computer Science

University of California, Los Angeles, 1997

Professor Walter J. Karplus, Chair

A study of validity of brain aneurysm blood flow simulation is presented. Five surgically constructed *in vivo* aneurysm models were used as the source of geometric and physiologic information. Methods for imaging, image processing, modeling and validation were reviewed and evaluated. Angiographic images of artificial aneurysms were used to reconstruct the 3–D geometry and to construct a physiologic model. Pulsatile flow of Newtonian blood through the aneurysm was numerically simulated using commercial computational fluid dynamics software. Simulated flow was compared with cineangiograms and Doppler ultrasonic measurements of flow in the animal models. Qualitatively, the simulated flow matched the experimental data as well as the results of previous *in vivo*, *in vitro* and numerical studies. Quantitative validation was inconclusive due to high uncertainty of the physiologic model.

# CHAPTER 1

# Introduction

This thesis will address computational methods that may provide insights into the usage of a new therapy for brain aneurysms. Aneurysms are considered a dangerous pathology as they are prone to develop ruptures that cause hemorrhage with often fatal consequences. It was estimated that the annual rate of deaths caused by aneurysm ruptures in North America exceeds 14,000 and intracranial aneurysms cause most nontraumatic subarachnoid hemorrhages and 20–25% of all intracranial hemorrhages [PLZ79].

The Computer Science Department and the Department of Radiological Sciences of the University of California, Los Angeles are collaborating in a joint project that combines computer science visualization and simulation techniques with medical image information processing and storage capabilities. The goal of the project is to develop tools that assist physicians in understanding and visualizing vascular anatomy and blood flow, improve training, and allow for better prediction of therapeutic outcomes.

The project includes:

- acquisition and archival of digital angiographic images.
- bulk blood flow quantitation.
- determination of blood vessel geometry, including generation of a 3-D model

of the aneurysm.

- Computational Fluid Dynamics (CFD)–based simulation of blood flow inside the aneurysm.
- virtual reality visualization of the simulation results.
- validation of the models and simulation results.

Significant progress has already been made, certain parts of the project are already implemented. Namely, Michael Harreld performed initial flow and simulation validation studies [Har93], developed a virtual reality visualization tool and performed follow–up validation studies [Har96]; Nicki Sonpar and Branko Marovic developed geometric modeling software [Son97, Mar96, Mar97] and Damon Liu proposed a software architecture for a database storing simulated data [Liu97]. This thesis will address validation studies and pre–simulation steps as necessary for validation purposes.

## 1.1 Importance of the Project

### 1.1.1 Intracranial Aneurysms

A vascular aneurysm is a "circumscribed dilatation of an artery, or a blood-containing tumor connecting directly with the lumen of an artery"[Ste95]. A typical saccular aneurysm is shown in Figure 1.1.

Most intracranial aneurysms are located on the circle of Willis – an arterial loop at the base of the brain that connects the two internal carotid systems (see Figure 1.2). Osborn [Osb80] reported that approximately 30% of intracranial aneurysms occur on the anterior communicating artery, 20–30% between the

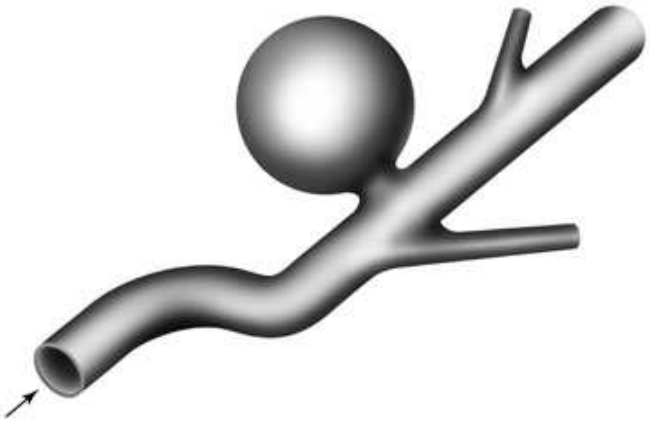

Figure 1.1: A saccular aneurysm.

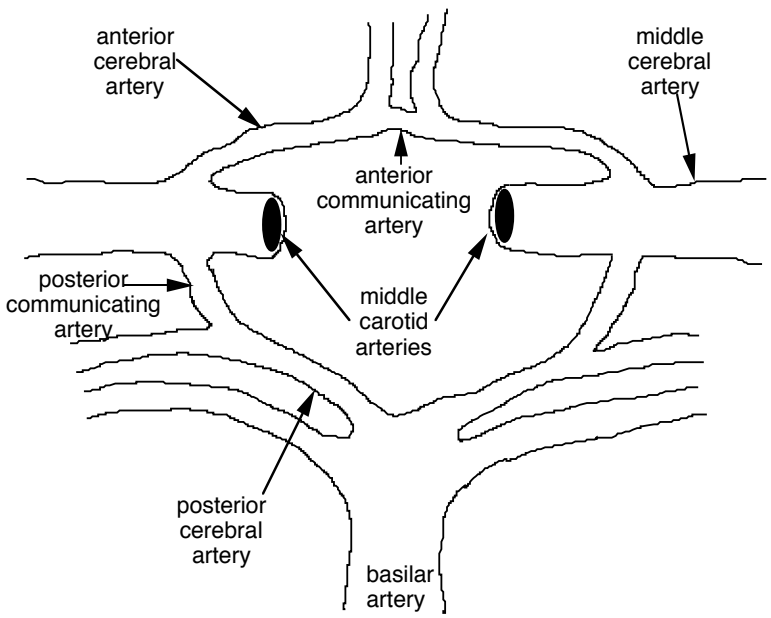


Figure 1.2: Schematic of circle of Willis with major arteries designated.

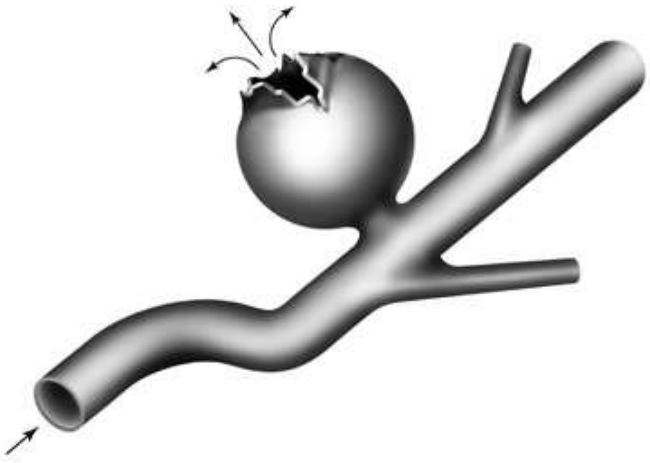

Figure 1.3: A ruptured aneurysm.

interior carotid and posterior communicating arteries, 20% on the middle cerebral artery bifurcation, and 15% from the basilar tip. A ruptured aneurysm (Figure 1.3) can cause a catastrophic hemorrhage with resulting death of the patient. We already mentioned that 20–25% of all intracranial hemorrhages are caused by intracranial aneurysms. Non–ruptured aneurysms have also been associated with many illnesses including headaches, migraines, loss of vision and neurologic disorders.

The incidence of aneurysms reported by various pathological studies varies between 0.2 and 10% depending upon investigator experience, autopsy purpose and the group of patients on which the autopsies are performed [PLZ79], [Fox83].

Aneurysms can be classified by their form and size. The most frequently encountered types of aneurysms are: [PLZ79]

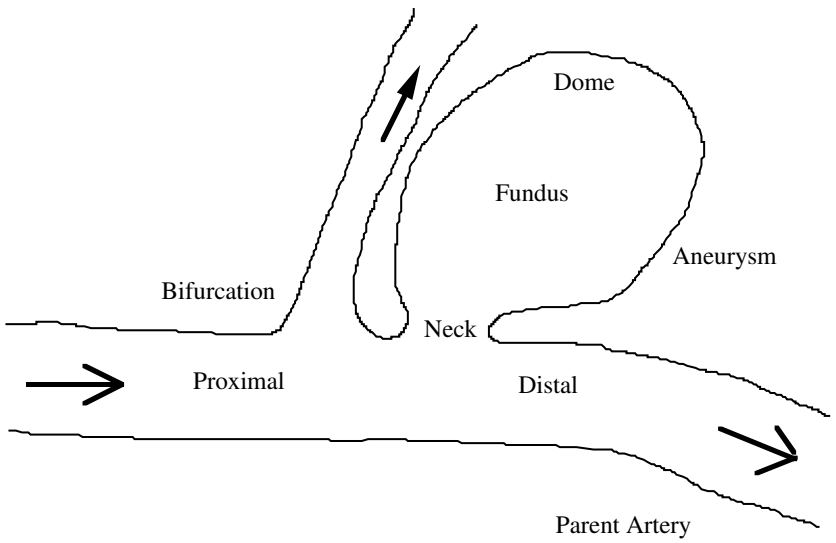


Figure 1.4: Schematic of bifurcation aneurysm with anatomic terms.

1. **Saccular (berry) aneurysms** (Figure 1.1): the most widely observed type of aneurysms is a saccular dilation of an artery connected to it by a neck or a wide attachment. They account for 66 – 90% of all encountered aneurysms vary in size between 2 and 50 $mm$. Typically, large aneurysms (2.5 cm in diameter or larger) are less rupture-prone and more susceptible to thrombosis. Aneurysms 5 to 15 mm in size are most likely to bleed or rupture [Ram87].

   Major subtypes of saccular aneurysms include:

   (a) **bifurcation aneurysms** – where an aneurysm develops in the place where a small artery forks off a larger one (Figure 1.4),

   (b) **terminal aneurysms** – where an aneurysms develops in the place where a large artery divides into two smaller ones, and

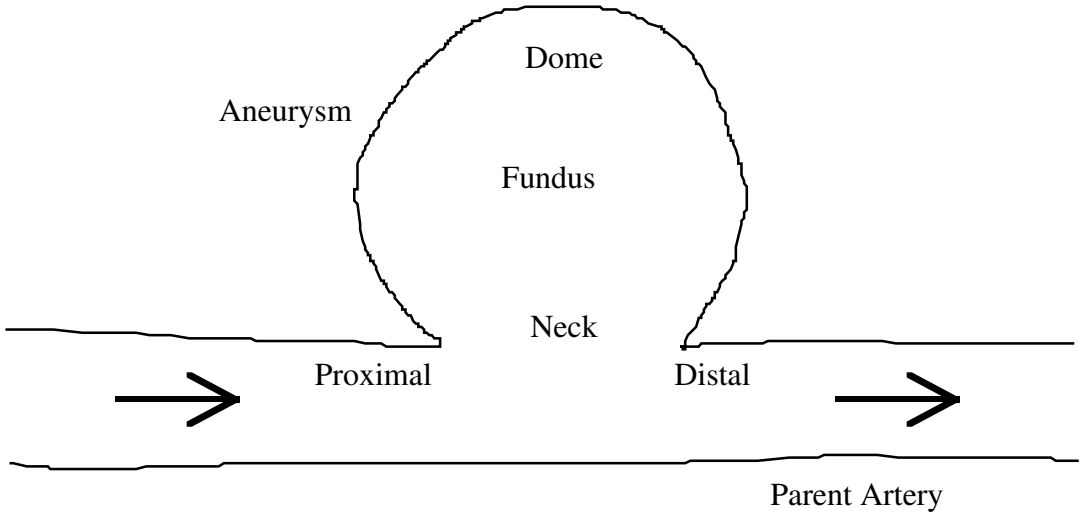


Figure 1.5: Schematic of lateral wall aneurysm with anatomic terms.

(c) **lateral wall aneurysms** – where an aneurysm develops on arterial wall far from any artifacts (Figure 1.5).

The first two subtypes account for more than 75% of brain saccular aneurysms due to complex geometries of vessel bifurcations and high velocity flow jets of a pulsatile nature oriented oriented perpendicular to the wall [AET93];

2. **Fusiform (atherosclerotic) aneurysms** (Figure 1.6) account for 6% – 16% of all encountered aneurysms and present an increase in diameter of the local artery;

3. **Dissecting Aneurysms** are very rare and are caused by a dissection of the arterial wall;

4. **Mycotic Aneurysms** account for 1% – 12% of all encountered aneurysms and are developed by bacteria or fungi lodging in the vessel wall.

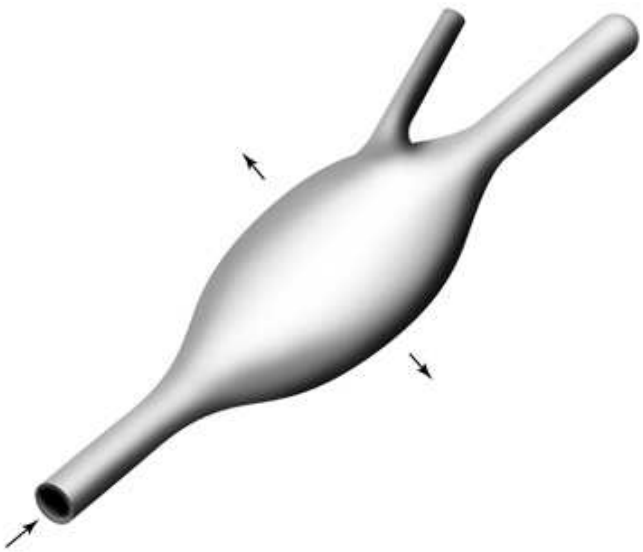

Figure 1.6: A fusiform aneurysm.

An alternative classification is based on thickness of the neck and the dome. A clinicopathological study found that neck thickness varies between 20–550 $\mu m$ and dome thickness is bounded within 30–500 $\mu m$. About 60–70 % aneurysms have irregular dome thickness [PLZ79].

The regions and terms in lateral wall aneurysms are illustrated in Figure 1.5.

### 1.1.2 Causes

The factors causing aneurysms, and the mechanisms of their growth, are being actively researched. The two most popular theories are the congenital theory, which holds that aneurysms are caused by inherited weaknesses of vascular walls, and the degeneration theory, which stipulates that aneurysms are created by acquired factors such as atherosclerosis and hemodynamics. Local hemodynamic

features have been found to be at least partially responsible for aneurysm creation, especially in the circle of Willis [LSP87]. Most researchers believe that aneurysms are caused by a combination of these factors, and that the growth of small aneurysms is a result of blood pressure and the pounding effect of pulsing blood against a wall which lacks the elasticity of typical blood vessels. As the aneurysm develops, the flow within the dilatation dilates the sac even further [PLZ79].

### 1.1.3 Symptoms and Detection

The typical symptoms of aneurysm–related illnesses include severe headaches, dizziness, nausea, blindness and neurologic disorders including decreased cerebral function, stupor and coma secondary to subarachnoid hemorrhage [PLZ79], [Ram87]. Between 12,000 and 28,000 U.S. patients suffer from aneurysm–related subarachnoid hemorrhages every year [MD95]. Over half of these patients die within thirty days after the hemorrhage and approximately one half of survivors suffer a permanent stroke caused by the blood from the hemorrhage irritating the brain blood vessels, causing them to become more narrow and eventually close in a "vasospasm." Figure 1.7 illustrates a vasospasm by showing a ruptured aneurysm releasing blood into the subarachnoid space in the left–hand part of the figure and the resulting constriction of many neighboring arteries that effectively cuts blood supply to the brain, as shown on the right–hand side of the figure.

Diagnostic medical imaging of the brain vasculature is typically performed when the above–mentioned symptoms occur or as a routine check–up. Angiography is the modality most commonly used to detect and locate intracranial

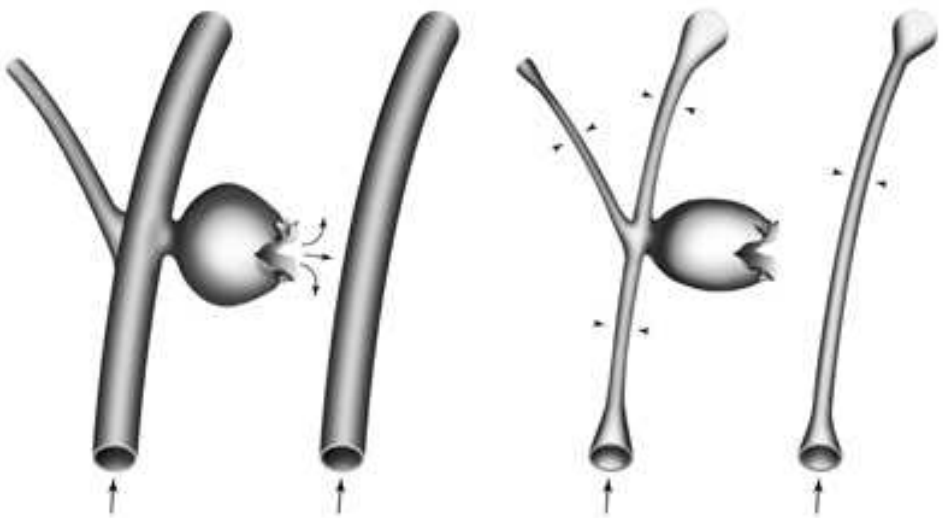

Figure 1.7: Vessel in vasospasm

Connected and neighboring blood vessels with aneurysm rupture in the left artery.

All arteries in vasospasm after aneurysm rupture. Artery constriction shown by little arrows.

aneurysms since it is the most efficient in producing the following information [PLZ79]:

- Identification and location of the aneurysm;
- Size and number;
- Neck configuration;
- Spasm evidence;
- Relation to other arteries.

Unfortunately, the two–dimensional nature of X–ray angiograms and the diffusion of contrast bolus makes it difficult to determine hemodynamic parameters of blood flow using angiography. On the other hand, CT and MR scans tend to be inefficient in aneurysm detection, especially if an acute subarachnoid hemorrhage has developed around the aneurysm [Ram87]. More hemodynamic information can be provided by intravascular ultrasonic flow meters but the usage of such invasive methods adds additional risk to clinical procedures [Ram87] and may corrupt the flow that they are intended to measure [DCP92].

### 1.1.4 Treatment

Any discovered aneurysms must be treated in a way that prevents them from rupturing and bleeding or stops bleeding if the aneurysm has already ruptured. The most popular method of aneurysm treatment is surgical clipping, which is based on placing a metal clip around the neck of the aneurysm to prevent blood from entering it and subsequently collapsing the isolated aneurysm [PLZ79]. Other surgical techniques for aneurysm treatment are used whenever clipping is not

feasible; these include wrapping the aneurysm with some material, bipolar coagulation of the aneurysm neck and carotid artery ligation. It is worth mentioning that all of these treatment techniques require the surgeon to approach the aneurysm from outside (extravascular approach).

A brain aneurysm is especially dangerous since its rupture may result in brain hemorrhage, intracerebral hematoma with subsequent cerebral emboli and strokes and it is likely to be concealed within the brain thus preventing the surgeons from attempting to close it from the outside using conventional treatment techniques.

The introduction of microcatheters that can be navigated through the arteries of the circle of Willis into the aneurysm has made it possible to perform endovascular (from within the vessel as opposed to from outside the vessel) treatment of aneurysms. A procedure based on inserting very soft platinum coils used to partially or completely block blood flow inside the aneurysm, and thus effectively close it, was developed in UCLA Department of Radiological Sciences and is performed there on regular basis [GVD92],[GJM94].

The technique is based on inserting a microcatheter with a metallic guide wire into a groin artery of a patient and navigating it through the carotid and circle of Willis into the aneurysm (Figure 1.8). Angiography is used as the primary method of monitoring the relative locations of the aneurysm, microcatheter and platinum coils. As soon as the target is reached, the guide wire is replaced with a stainless steel wire that delivers the attached platinum coil into the aneurysm. When the coil fills the aneurysm completely (Figure 1.9), a positive direct electric current is applied to the guidewire, initiating an electrolysis process that attracts, on the one hand, negatively charged blood components to the platinum coils, thus promoting clot creation and dissolving, on the other hand, the uninsulated

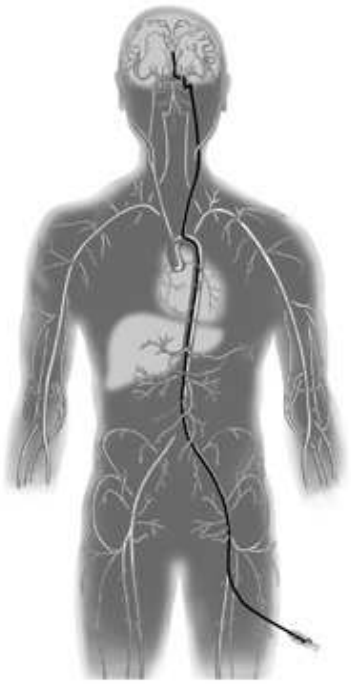

Figure 1.8: Path of microcatheter for endovascular brain aneurysm treatment.

Figure 1.9: Occlusion of an intracranial aneurysm with platinum coil.

end of the guidewire thus detaching the coils within the clotted aneurysm. At this step both the delivery wire and the microcatheter can be removed and the treatment is complete. Angiography is also used to monitor the movements of the delivery wire and the process of filling the aneurysm with platinum coils. It is necessary to mention that the variety of aneurysm sizes and shapes requires interventional radiologists to select size and number of coils appropriate to treat every given aneurysm on an individual basis [GVS91], [GVD91]. Eventually progressive thrombosis develops on the coils and completely fills in the aneurysm, effectively blocking any flow inside it thus significantly reducing the chances of rupture.

Alternative endovascular treatment techniques include the use of detachable balloons and the injection of liquid occlusion material. There methods tend to require more preparatory stages, to be inefficient for small aneurysms and

to present higher degree of danger to patient than coil–based electrothrombosis [TNY92].

However, electrothrombosis techniques may result in the aneurysm being ruptured by a hydraulic blow or by the coils themselves, the coils might not reduce the blood flow towards the most endangered regions of the aneurysm sufficiently to prevent a rupture or surplus coils might stay in the artery outside of the aneurysm and block the flow through the affected artery. All these possible dangers demand quality prediction of the outcome of chosen treatment that, in turn, can be assisted by performing computer simulations of the endovascular procedures.

## 1.2 Digital Radiology

The advances in digital computer technology and their increasing integration in the clinical environment allows to improve or substitute for some traditional methods with computer–based ones. For example, picture archiving and communications systems (PACS) have been found to provide accuracy and efficiency superior to pre–digital radiographic techniques [LH92]. Moreover, digital clinical equipment allows an automated or a semi–automated interface with other computers providing different services using either local– or wide–area network connections.

Digital radiology typically performs studies using various modalities and stores the results in digital form. Below we will provide a short description of the UCLA PACS used for the purposes of this project [HTL93],[HT92].

The components used in this study are located at the Leo G. Rigler Cen-

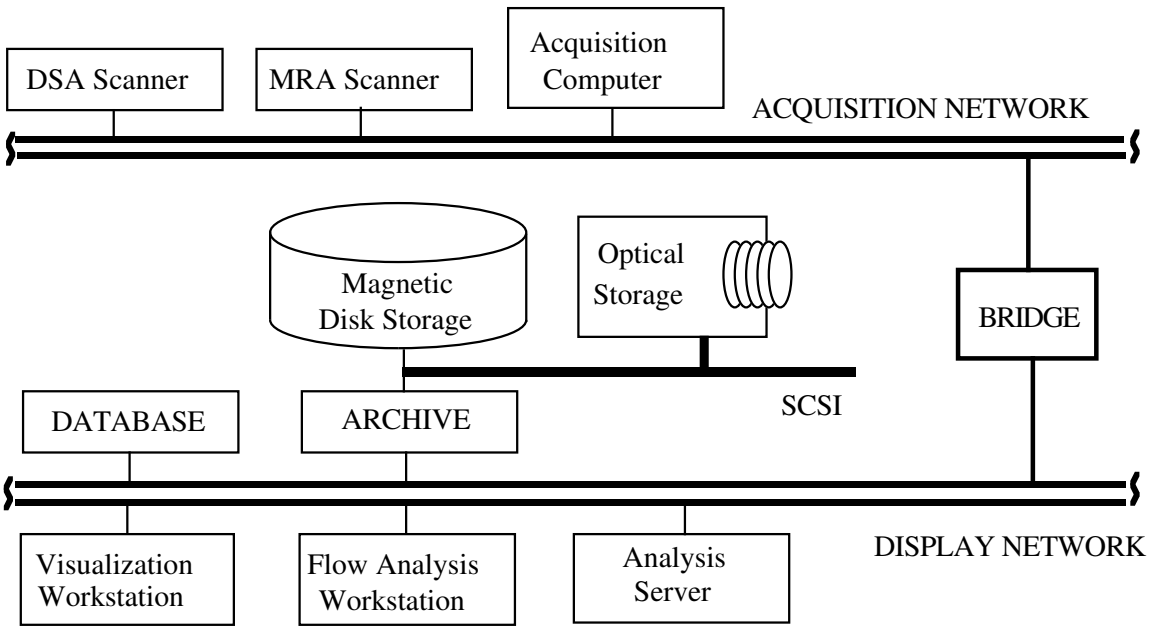


Figure 1.10: UCLA PACS Architecture.

ter and Image Processing Laboratory of the UCLA Department of Radiological Sciences. All acquisition systems (e.g. DSA, MRI/MRA, CT scanners and acquisition computers) are connected to an acquisition network based upon an Ethernet backbone (Figure 1.10). A bridge connects the acquisition network to the display network, which connects visualization and analysis workstations to the image database and large–scale image archive.

## 1.3 Scope of Investigation

The main goal of this research was to study the validity of computer simulations of brain aneurysm blood flow by comparing *in–vivo* and numerical results and to study, evaluate and integrate computational techniques that can automate the

process of preparation and execution of a simulation.

The simulation preparation can be divided into the following successive steps:

- acquisition of geometric and physiologic data,
- data preprocessing and segmentation, if necessary,
- 3–D geometric modeling,
- construction of a geometric model acceptable for the CFD solver used,
- quantitation of the blood inflow into the model to be used as the boundary condition for the simulation, and
- construction of a physiologic model for validation purposes.

After the simulation is prepared, the following steps can be designated:

- blood flow simulation using the derived geometric and physiologic models, and
- validation studies.

Every one of the above–listed steps requires that the following be done:

- available methods, algorithms and software will be studied, compared and evaluated, if necessary,
- if no software is available or suited for any part of the project, it will be developed, and
- all available software including commercial, freeware and locally developed code will be integrated into a suite of programs.

In addition, validation studies require knowledge of blood flow inside the whole parent artery–aneurysm complex.

We will limit the scope of physical models of aneurysm blood flow by making a number of assumptions such as considering blood to be a non–Newtonian fluid, the artery and aneurysm walls to be inelastic and the flow to be non–turbulent. The model assumptions will be investigated in full detail in Chapter 2. We will also limit the scope of the validation study by selecting an intravascular Doppler flow meter as the primary source of flow velocity information and digital X–ray cineangiograms as the secondary one.

## 1.4 Organization

This thesis is divided into 6 chapters including this introduction and conclusions. Specifically, Chapter 2 reviews aneurysmal blood flow studies, mathematical models and numerical simulations; Chapter 3 describes brain aneurysm models as well as the sources of geometry and flow data; Chapter 4 focuses on a literature review for image processing methods while Chapter 5 discusses the simulations performed and their results .

# CHAPTER 2

# Brain Aneurysm Blood Flow

## 2.1 Previous Studies

The problem of blood flow in intracranial aneurysms has been widely investigated. Published studies include computer simulations, flow phantom studies and *in vivo* measurements. Studies of blood flow through aortic aneurysms have also been performed and were surveyed as they are physiologically and geometrically close to intracranial aneurysms despite tending to be considerably larger.

Perktold et al. [PKH88] observed numerically simulated incompressible non–pulsatile Newtonian blood flow circulate in a whirl within simulated intracranial aneurysms.

Perktold, Peter et al. [PPR89] performed a numerical simulation of pulsatile Newtonian and non–Newtonian blood flow through a vessel with a saccular intracranial aneurysm. They found the intra–aneurysmal flow circulation to be relatively slow in comparison with the flow in the parent vessel. The flow into and out of the aneurysm was also slow.

Matsuzawa [Mat93] observed multiple separation vortices occurring while numerically simulating steady blood flow through a lateral wall aneurysm. The vortices were distorted by the geometrical shape of the aneurysm. The number and size of these vortices was found to depend upon the flow velocity.

Steiger et al. [SPL87] studied blood flow in physical models of lateral wall aneurysms and found the basic pattern of intra–aneurysmal flow circulation to be independent of the size of the aneurysm phantom. Local disturbances of laminar pulsatile flow were observed in some models at physiologically realistic Reynolds numbers, but no turbulence was reported.

Kumar and Naidu [KN95, KN96] studied numerically simulated pulsatile flow of Newtonian blood through a fusiform aneurysm. They observed multiple flow recirculation and stagnant fluid regions, changing positions, sizes and shapes, appearing and disappearing with time.

Liepsch et al. [LSP87] found the flow of pulsatile Newtonian and non–Newtonian fluids through glass and silastic aneurysm models to enter the aneurysm near its distal lip. The flow inside the aneurysm was directed towards the center of the fundus and exited the aneurysm along the side walls. The flow velocities in the center of the aneurysm were as low as $0.4 - 2$ % of the velocity in the parent vessel in the steady case and as low as $8 - 13$ % in the pulsatile case. The flow inside the aneurysm was considered to depend upon the velocity and degree of pulsatility of the flow in the parent vessel as well as blood viscosity.

Austin et al. [AS95] performed a biomathematical simulation of pulsatile Newtonian brain aneurysm blood flow, based on an electric circuit model. The flow was found to display discontinuous jumps in velocity amplitude at certain frequencies.

Low et al. [LPR93] studied numerically simulated three–dimensional pulsatile flow of incompressible non–Newtonian fluid though rigid and distensible lateral wall aneurysms located on both straight and curved arteries. They supported the findings of Liepsch [LSP87] that the intra-aneurysmal flow pattern started from

the distal lip, proceeded backwards through the center and left the aneurysm along the sidewalls. The flow speeds inside the aneurysm were found to be an order of magnitude lower than the arterial speeds. With a distensible wall, the intra-aneurysmal flow increased somewhat, mostly due to a significant increase in the secondary flows (oriented across the axis of the parent vessel). The greatest expansion and contraction of the aneurysm wall was found in the neck near the distal lip of the aneurysm where the fluid flow enters.

Niimi et al. [NKS84] observed significant secondary flows in a physical model of an asymmetrical saccular aneurysm adjacent to a curved artery.

Strother et al. [SGR92] imaged blood flow in experimental canine aneurysms using digital subtraction angiography and color Doppler. The flow was found to be laminar or transitional rather than turbulent. It entered the aneurysm near the distal lip as a fast narrow jet surrounded by a slow–velocity region and slowly left it near the proximal lip. Regions of stagnant fluid were found in the center of the fundus. The flow and the hemodynamic stresses were found to vary between aneurysms, depending upon the shapes of the aneurysms and their necks.

Gonzalez et al. [GCO92] found vortices of numerically simulated pulsatile two–dimensional non–Newtonian aneurysm flow to reverse direction during a heart cycle. During systole, blood was entering the aneurysm along the proximal wall and leaving along the distal one. During diastole, the flow pattern was reversed.

Ortega [Ort96] used a commercial CFD solver *FIDAP 7.0* (Fluid Dynamics International, Evanston, IL) to numerically simulate pulsatile flow of Newtonian blood through *in vivo* cerebral aneurysm models. The aneurysm models were surgically constructed in live rabbits. Blood flow was observed to change direction

during the heart cycle. During diastole, blood was entering the aneurysm near the proximal lip, circulated in a small vortex near the proximal side and left the aneurysm along the distal wall. During systole, the vortex grew is side until it started dominating flow in the aneurysm. Flow separation was observed near the proximal neck. The numerical results were found to match color Doppler ultrasonic flow velocimetry measurements.

Schrader et al. [SPB92] observed steady fluid flow through a physical model of a fusiform aortic aneurysm using Color-Doppler Flow Imaging and found the flow pattern to change from smooth and laminar to irregular and turbulent with increase of flow velocity. They noted that this conclusion corresponds with clinical observations.

Taylor et al. [TY94] observed vortices of numerically simulated pulsatile Newtonian aortic aneurysm blood flow to change position and shape, and appear and disappear with time.

Matsuoka et al. [MSO92] studied blood flow patterns in relatively large human aortic aneurysms using cine 2–D Phase–Contrast Magnetic Resonance Angiography (PC MRA). They observed a multitude of flow patterns ranging from irregular to circular flow. They also observed chaotic turbulent flow inside some aneurysms. Larger aneurysms tended to demonstrate lower but more regular flow, flow through the smaller ones tended to be irregular or break into multiple independent circulation vortices.

Unfortunately, the studies surveyed lack generality, tend to disagree and sometimes suffer from unreasonable assumptions. For example, some researchers assumed that secondary flows are negligible and that flow can be modeled as two–dimensional, which is contradicted by the results of Niimi et al [NKS84], Low

et al [LPR93] and others. Despite the disagreements, certain observations were supported by multiple researchers. Most flow patterns had aneurysm inflow near the distal lip and slow recirculation or regions of stagnant fluid in the center of the fundus. Many researchers reported flow patterns to depend upon flow velocity, degree of flow pulsatility phase of the simulated heart cycle. Multiple recirculation vortices were seen to change position and shape, and to appear and disappear. Reports of turbulent flow inside aneurysms are relatively rare, as opposed to reports of low-speed laminar or transitional intra–aneurysmal flow.

To summarize this survey, it can be stated that no general model of aneurysmal blood flow has been presented so far. It may be that the variety of aneurysm shapes and blood flow regimes do not allow for one general model of intracranial aneurysm blood flow to be created. In this case, a set of models for different geometric and physiologic conditions must be used.

## 2.2 Mathematical Model

In this section the assumptions and simplifications that were made will be described, as well as the resulting mathematical model used to simulate brain aneurysm blood flow.

### 2.2.1 Assumptions

Several assumptions were made in order to simplify the computer model of a swine aneurysm, including:

1. **Coarse geometry.** The geometry of the aneurysm and the adjacent artery is somewhat coarse due to the large size of hexahedral blocks employed

to create a model for *NEKTON* and due to the low spatial resolution of the DSA–based geometry reconstruction algorithm. This assumption is acceptable since the sharp corners of the model would be effectively rounded and smoothed by the stagnant fluid collecting there.

2. **Inelastic aneurysm and artery walls.** The assumption is reasonable since the angiograms of experimental swine aneurysm show only small movements of artery and aneurysm walls. Visual observations of experimental aneurysms support the validity of this assumption, but an imaging method with higher spatial and sufficient temporal resolution may provide more information on wall elasticity. Chitanvis et al [CHP95] found that wall elasticity affects simulated Newtonian and plastic (non–Newtonian shear–thinning) flows through aneurysms but noted that supporting *in vitro* experiments and *in vivo* observations have yet to be conducted. Pedley [Ped95] concluded that wall elasticity slightly reduces wall shear but may result in non–unique stable solutions dependent upon initial conditions.

3. **Non–turbulent blood flow.** This assumption is reasonable for an initial study and may be correct for low-speed blood flow in a straight artery. The onset of turbulence (chaotic movement of fluid in space and time) is usually predicted using the Reynolds number $Re$, defined as

$$Re = \frac{\delta \cdot u}{\nu} \tag{2.1}$$

where $\delta$ is the characteristic dimension, $u$ is the local flow velocity, $\nu = \frac{\mu}{\rho}$ is the kinematic viscosity, $\mu$ is dynamic viscosity and $\rho$ is fluid density [Whi74]. The flows measured in the proximals of experimental aneurysms can be characterized by values of $Re$ ranging between 600 and 3000. Reynolds

demonstrated that flow of fluid through a long straight cylinder will remain non-transient as long as the Reynolds number is below 2000 [Rey83, Whi74]. The maximal Reynolds number that still ensures laminar flow is called the critical Reynolds number $Re_c$. It was also shown that turbulence of the freestream does not affect the value of the critical Reynolds number but increases the intermittency factor (percentage of turbulent flow) after the transition point. Surface roughness, bifurcations and vessel twists are known to reduce the critical Reynolds number, but there is no single exact numerical criteria of such reductions [FR72]. Single 2–D roughnesses of size up to 30% of numerical boundary layer thickness $\delta^*$ were shown not to disturb the flow in the boundary layer. A single 3–D roughness of height up to $0.6 \cdot \delta^*$ should not disturb flow sufficiently to change $Re_c$ [Whi74]. A rough (sand–grain wall) pipe can be considered smooth if the average roughness $k$ is less than $\frac{10 \cdot \delta}{Re}$ [Whi91]. On the other hand, since blood is a thixotropic fluid (its viscosity decreases under increasing shear and gradually recovers when the shear is removed) and can be pumped at high rates with a pressure drop lower than in a corresponding Newtonian fluid, its transition to turbulence occurs at Reynolds numbers much higher than for a corresponding Newtonian fluid. It was shown that the transition period for thixotropic fluids does not start until Reynolds numbers as high as $50000 - 70000$ [Din85]. In addition, Buss demonstrated that for pulsatile flows, the critical Reynolds number is dependent upon flow speed oscillation frequency in a direct proportion [Bus83]. The considerations above allow arterial flow of healthy blood to be treated as laminar, unless turbulence is observed.

4. **Constant blood viscosity.** In the conducted simulations, blood viscosity was assumed to be a constant despite the fact that blood is an inherently non–Newtonian fluid with viscosity dependent upon shear rate and time [Din85]. The assumption is still reasonable as a coarse approximation since the changes in viscosity are low in comparison with the absolute value and the literature gives varying values for viscosity. In addition, Perktold et al [PPR89] numerically simulated pulsatile flow of Newtonian and non–Newtonian blood through a bifurcation with an aneurysm and reported no significant differences. However, Harreld [Har96] contradicts this observation by reporting numerically simulated pulsatile flow of Newtonian and non–Newtonian blood through a lateral wall aneurysm to differ significantly in both average value and velocity profile.

5. **No heat transfer.** This assumption is valid as the blood temperature changes over the small region of interest are expected to be insignificant.

6. **Incompressible fluid.** The assumption is reasonable for flow speed well below the speed of sound which are typical for arterial blood flow.

7. **No–slip boundary conditions.** For any flow of a viscous fluid along a rigid wall, the flow velocity is equal to zero at any point on the wall (i.e. no fluid slippage on the wall is observed) [Whi91]. As the aneurysmal and arterial walls are assumed to be rigid and blood is assumed to be viscous, the no–slip boundary condition assumption is reasonable.

### 2.2.2 Formulation of Characterizing Partial Differential Equations

The model can be characterized as three-dimensional transient laminar flow of incompressible Newtonian fluid without heat transfer through a rigid vessel with non-slip walls. Such flow is governed by the laws of momentum and mass conservation. The governing partial differential equations and the initial and boundary conditions of the model will be described below.

#### 2.2.2.1 Navier-Stokes Equation

The Navier-Stokes equation describes conservation of momentum in a viscous fluid and is written [Whi74, Flu92] as:

$$\rho(\frac{\partial \vec{v}}{\partial t} + (\vec{v} \cdot \nabla)\vec{v}) = -\nabla P + \mu \nabla^2 \vec{v} \tag{2.2}$$

where $\vec{v}$ is the velocity vector, $\rho$ is fluid density, $P$ is pressure, $\mu$ is viscosity and the symbol $\nabla$ stands for the gradient operator. Viscosity is considered to be a constant for a Newtonian fluid. Following Patankar [Pat90], we will describe the four terms of the equation 2.2 as the change of momentum with time, momentum convected into a small volume by the flow, change of momentum over time due to net pressure forces and the momentum change over time caused by friction-induced shear forces respectively.

#### 2.2.2.2 Continuity Equation

The equation of continuity describes conservation of mass and for an incompressible flow can be written [Whi74, Flu92] as:

$$\nabla \cdot \vec{v} = 0 \tag{2.3}$$

It can be described as setting the sum of inputs and outputs to and from an infinitely small element equal to zero.

#### 2.2.2.3 Constitutive Equation

Newtonian fluid can be characterized by a direct proportion between the shear stress and strain rate. For a two–dimensional model, the dependency can be written [Whi74, Pat90] as:

$$\tau = \mu\dot{\gamma} \tag{2.4}$$

where $\tau$ is the shear stress, $\gamma$ is the strain rate and $\mu$ is viscosity.

For non–Newtonian thixotropic fluids such as blood, viscosity becomes a function of both shear stress and time. The non–linear relation between shear stress and strain rate is called constitutive equation and must be solved for the whole flow field. Among the possible models of non–Newtonian viscosity is the power law model which in two–dimensional case can be written [Whi74] as

$$\tau = K\dot{\gamma}^n \tag{2.5}$$

where constant $n$ is the power (for $n = 1$, the constitutive equation is Newtonian) and $K$ is a constant representing the actual viscosity if $n = 1$.

#### 2.2.2.4 Boundary Conditions

The boundaries $\Gamma$ of the model consist of the wall $\Gamma_w$, the inlet of the proximal $\Gamma_i$ and the outlet of the distal $\Gamma_o$, where $\Gamma = \Gamma_w + \Gamma_i + \Gamma_o$. We will use both Dirichlet and Neumann boundary conditions, the former for the boundaries where only the velocity is specified and the latter for the boundaries where only traction is given.

For $\Gamma_w$ a Dirichlet boundary condition was used since the assumption of rigid

walls with no velocity slip allows to set velocity on the walls equal to zero.

The simplest boundary condition for $\Gamma_o$ is to assume that the velocity profile stabilizes downstream of the aneurysm. Such assumption is reasonable if a distal vessel of sufficient length is attached to the aneurysm. Stable distal velocity allowed the use of a Neumann boundary condition of constant zero pressure on the outflow surface $\Gamma_o$.

For $\Gamma_i$ a Dirichlet boundary condition based upon the measured flow velocity on the surface of the inlet was used. If the flow is pulsatile and the flow velocity is measured as a function of time, a time–dependent boundary condition can be implemented. It is important to note, however, that flow velocity data must be measured in every point of the inlet surface, thus creating essentially a flow velocity profile. As the sampling volume of the intravascular Doppler probe is comparable in diameter with the vessel (see Section 3.3.2), the hemodynamic information available was limited to flow velocity averaged over the arterial cross-section. In order to solve the problem, $\Gamma_i$ was moved upstream and the input velocity was assumed to be transient plug flow. As long as the inlet is sufficiently long for the flow to develop in full by the time it reaches the aneurysmal neck, the profile of flow velocity there will be close to the real one. An estimate for the minimal length of such intake was given by [CPS78] as

$$X = 0.03d \cdot Re \tag{2.6}$$

where $X$ is the proximal length, $d$ is the diameter of a straight artery, $Re$ is Reynolds number and 0.03 is an experimentally derived constant. The plug flow velocity must be selected in such a way that the mass flow will remain unchanged, which, in case of parabolic cylindrical flow, is one half of the maximum velocity measured by intravascular Doppler [Har93].

#### 2.2.2.5 Initial Conditions

Since the flow is transient, the initial conditions which describe a starting field of velocities within the boundaries $\Gamma$ provide a starting point for the solution on the first time step. For a steady–state flow, initial condition importance is negligible and it is reasonable to start the solution with a zero velocity field. For a periodic pulsatile flow, the optimal initial condition is the solution on the time step immediately before the first. If such a solution is not available, a reasonable guess should be used and later replaced by the solution obtained at the end of the period. This solution should be used as the initial guess for the next iteration of the solution process.

However, a highly iterative solver will quickly overcome the influence of an inaccurate initial velocity field. In fact, *NEKTON* simulations were conducted over 1.5 heart cycles and demonstrated that the solutions obtained in the first halves of the first and second heart cycles are similar, especially in the second quarters of the cycles. This indicates that it is reasonable to start the solution with a zero velocity field and avoid the lengthy process of iterative determination of optimal initial conditions.

### 2.2.3 Blood Properties

The blood density was considered to be equal to 1240 $kg/m^3$. The dynamic viscosity was selected as 30 centiPoise, which is typical for healthy swine blood [Din85].

## 2.3 Numerical Methods

A number of numerical methods are widely used to solve Navier–Stokes problems on digital computers. In this section these methods will be surveyed and compared in order to find which method is best suited for the simulation of blood flow through brain aneurysms.

### 2.3.1 Survey of Numerical Methods

Numerical methods are typically compared using such criteria as speed of convergence, accuracy, computational expenses in terms of both CPU time and memory requirements, applicability for the problem under consideration (for non–general methods), ease of use and implementation.

#### 2.3.1.1 Finite Difference Method

The FD method is based on approximating derivatives by finite differences. While simple in implementation and theory, the method is inefficient for complex geometries and unstructured grids [Pat90].

#### 2.3.1.2 Control Volumes Method

The control volumes method (CVM, also known as the finite volume method, or FVM) is based on integration of fluxes through the faces of a control volume created around a node of an orthogonal (Cartesian, polar or body-fitted) grid. The full set of distinct control volumes completely covers the computational domain. The vector solutions are calculated on the volume faces, scalar solutions are calculated in volume centers (grid vertices) [Flu95]. The method is highly ef-

ficient for high–gradient flow, but is ill–suited for unstructured meshes and tends to produce solutions less accurate than the finite elements method [Pat90].

#### 2.3.1.3 Method of Weighted Residuals

The method of weighted residuals (MWR) is based on minimizing the "residual" – the difference between approximate and true solutions over a set of test functions. In this approach, an unknown approximate solution is substituted into the differential equation thus defining the residual, which is minimized by lowering the order of the equation (known as the transition to the "weak form") and setting the result to zero. A series of linear algebraic equations is generated by choosing a succession of weighting functions for the differential equation in the weak form. The system of algebraic equation is resolved for the unknown parameters that are used to calculate the solution [Sch88, Fro85].

Being a general method, MWR has a number of extensions that differ in their choice of the test and the basis functions used to expand the approximate solution over the computational domain. The finite element method, the spectral method and the spectral element method all belong to the MWR class.

#### 2.3.1.4 Finite Elements Method

The finite elements method (FEM) is a member of the MWR class widely used in a multitude of fields including computational fluid dynamics. The method is based upon dividing the computational domain into a set of distinct non–intersecting elements called "finite elements". The basis functions describe the variance of the solution over an element and are selected in such a way that the $i$-th basis function is equal to 1 at the grid node $i$, equal to 0 at all other nodes

and has a non–zero value only on the elements associated with the node $i$. The total solution is obtained by applying the weighting function to the set of basis functions.

FEM is considered to be well-suited for complex geometries and unstructured grids due to the high flexibility of its basis function mechanism and high accuracy. Numerous researchers have successfully applied it to simulate pulsatile and steady Newtonian and non-Newtonian flows in various aneurysms [KN96, KN95, PPR89, PFH88, Mat93]. However, the high computational expenses of FEM has forced many researchers to investigate possible alternatives [Pat90, Flu92].

#### 2.3.1.5 Spectral Method

The spectral method is another member of the MWR class of methods, which defines the basis functions on the whole computational domain so that they may have non–zero value over all nodes in the domain. Basis functions are typically approximated using Legendre or Chebyshev polynomials [CHQ88]. While the method achieves very fast convergence on simple problems, it is computationally expensive and difficult to use with complex geometries [Flu92].

#### 2.3.1.6 Spectral Element Method

The spectral element method (SEM) is a combination of FEM and spectral methods that combines quick convergence of the latter with the absence of geometrical limitations of the former. In SEM, the basis functions are defined over large subdomains called "spectral elements" that can assume complex shapes.

A typical implementation of SEM divides the computational domain into hexahedral spectral elements inside which Cartesian meshes of collocation points

are generated and the dependent variables are expanded over the collocation (local mesh) points. FEM techniques are applied to generate a linear algebraic system that is solved for local weighting functions [Flu92, CHQ88].

Among the other advantages of SEM over FEM are the relative ease of geometry generation due to large size of the user-created elements, smoother solutions due to more efficient approximation and the ease with which the density of the intra–element mesh can be changed by setting the number of collocation points per element. However, SEM assumes that the simulated flow is relatively smooth and has relatively low gradients, thus making it inapplicable to many high–gradient flows.

#### 2.3.1.7 Control Volume Finite Element Method

This combination of CVM and FEM creates control volumes around all nodes of the finite–element mesh. The value of a basis function associated with a node is set to unity over the control volume associated with its node and zero elsewhere, so the discretization of the differential equation involves the imposition of conservation laws on the control volumes. This property allows CVFEM to combine high accuracy and ease of accommodation of complex geometries typical for FEM with low computational expenses and high efficiency on high-gradient flows that characterize CVM [BP83, Flu94a].

#### 2.3.1.8 Boundary Element Method

The boundary element method allows the solution to be found in the interior of an element from the solution on the boundary using Green's theorem as the theoretical basis. As it is complicated and difficult to implement, its use so far

has been limited to flow regimes that can not be efficiently modeled using other methods, such as transsonic and boundary flow [BM90, Flu92].

### 2.3.2 Numerical Method Selection

Since the geometry of the simulated object is highly complex and the use of unstructured meshes is desired, the choice of numerical method is limited to certain members of the MWR class, namely classic Galerkin FEM, SEM and CVFEM. The primary disadvantage of SEM is its requirement which the flow simulated must have low gradients that may or may not be true in this case. The conventional FEM in the Galerkin form does not have such restrictions but has very high computational expenses and requires a much finer grid than SEM. The CVFEM does not seem to have major disadvantages except for requiring finer meshes that SEM, but it is a relatively new and unproven method.

Based upon the survey above, SEM was selected as the primary numerical methods provided that the flow gradients stay low. If they become relatively high, we should use either CVFEM or classic Galerkin FEM.

## 2.4 Simulation Software

### 2.4.1 The Initial Selection

The initial selection of CFD software was made in 1992 in favor of *NEKTON* (Fluent Inc., Lebanon, N.H.). The selection process and the criteria employed to evaluate competing commercial CFD products was described by Harreld [Har93]. The package uses spectral-element spatial and explicit Adams-Bashforth temporal discretization, and was designed for simulation of steady and unsteady

incompressible fluid flows [Flu92].

Performed simulations, however, proved that the selection was far from being optimal as the velocity gradients across the flow lines were found to be considerably high near the aneurysm vortices [Har93]. It can be argued that SEM may not be well-suited for simulation of fluid flow through a non–smooth object like a parent artery–aneurysm complex. In addition, *NEKTON's* mesh requirements described in Section 3.4.1 were found to be awkward and unduly restricting in efficient modeling of geometries with increasing complexity [Har96]. That, and the advances in CFD after 1992 called for a comparison between *NEKTON V2.85* and more contemporary simulation software.

### 2.4.2 Subsequent Changes

By 1995, *NEKTON V2.85* became somewhat outdated by then–modern CFD products. We decided to perform a comparison of industry–leading software packages using the same evaluation criteria as the ones used for the initial CFD software selection. The following products were compared:

- **NEKTON 3.0** (Fluent Inc., Lebanon, N.H.) is a slightly improved *NEKTON V2.85*, still based on SEM and capable of simulating Newtonian and non–Newtonian incompressible flows using structured grids.

- **Fluent 4.3** (also Fluent Inc., Lebanon, N.H.) is based on CVM capable of simulating Newtonian and non–Newtonian steady-state flows using either unstructured tetrahedral or structured meshes and simulating Newtonian and non–Newtonian unsteady flows using structured spatial grids. The package performed well in the 1995 CFD Triathlone [Fre95].

- **Fluent/UNS 4.0** (also Fluent Inc., Lebanon, N.H.) is a highly advanced CFD solver that can simulate unsteady Newtonian and non–Newtonian laminar and turbulent flows using adaptive unstructured tetrahedral meshes. The solver is based on a combination of CVM and FEM known as Control-Volume Finite Element Method (CVFEM) offering robustness and economy of CVM on unstructured meshes [Flu94a, Flu96].

- **Rampant 2.0** (also Fluent Inc., Lebanon, N.H.) is a FEM–based package designed to model compressible Newtonian fluid flows using either structured or unstructured meshes.

- **FIDAP 7.0** (Fluid Dynamics International, Evanston, IL) is also based on FEM and is capable of simulating Newtonian and non–Newtonian flow on structured meshes. A *FIDAP* solver for unstructured meshes was announced but unavailable.

- **Phoenics 2.2** (CHAM Ltd., London, Great Britain) is a powerful CVM–based package capable of simulating almost any type of flow using structured meshes.

Of the structured–mesh solvers, *FIDAP 7.0* was found to be the best choice because of being better-suited for simulating non–smooth flows than *NEKTON* by virtue of using FEM and being more convenient in use, and having better supported than *Phoenics*. Of the unstructured–mesh CFD packages, *Fluent/UNS* was the only applicable choice. Therefore, the choice was to be made between a structured- and an unstructured–mesh solver. As unstructured meshes are inherently more flexible and thus better suited for modeling objects of highly complex geometry, the unstructured–mesh solver *Fluent/UNS 4.0* was chosen as

the replacement for less capable *NEKTON 2.85* product. The transition from the latter to the former was finished by 1997.

# CHAPTER 3

# Brain Aneurysm Models

A complete brain aneurysm model is required to perform valid blood flow simulations. It must include the size and shape of the aneurysm and parent artery (a geometric model), and the velocity of the blood flow at the entrance into the simulated parent artery-aneurysm complex (a physiologic model).

## 3.1 Model Constraints

A number of constraints are imposed on the selection of aneurysms to be modeled by either physical reasons or limitations of the methods and equipment used.

### 3.1.1 Size of Object Features

Any method that can selected for geometric model construction is likely to have limited resolution. For example, at the time of this writing the best spatial resolution of MR–based imaging methods is limited to $0.5 - -1.5mm$ while the neck of the smallest aneurysms may be as small as 2–4 $mm$ in diameter. If an important feature of the aneurysm being modeled is smaller than the best resolution available, geometric information will be irrevocably lost. In order to avoid this possibility, the diameter of the parent artery, the diameter of the aneurysmal neck and the aneurysm itself must be larger than the resolution of

the imaging method used to obtain its geometry.

### 3.1.2 Flow Velocity Constraints

The aneurysm should be selected in such a way that the flow measurement methods employed to construct the physiologic model would be capable of providing both the average velocity and profile of the flow into the aneurysm. The most general restriction imposed by this constraint is that the flow into the parent artery–aneurysm complex should lie within the effective range of the flow measurement methods used.

## 3.2 Sources of Geometry Data

The information about the size and geometry of an aneurysm can be obtained in many ways. In this thesis, the following methods are evaluated and discussed:

- Visual observations and measurements,
- Digital Subtraction Angiography(DSA),
- Magnetic Resonance Imaging and Angiography(MRI/MRA),
- Computed Tomography(CT).

### 3.2.1 Visual observations and measurements

Visual observation is done by looking at the aneurysm, measuring its dimensions with a ruler, visually estimating its shape and recording the obtained data on paper. This procedure only provides an approximate external view of the aneurysm, while at the same time requiring the aneurysm be exposed to external

observation, which defeats the purpose of endovascular treatment. While visual observation is useful in helping a human operator obtain a general understanding of the shape of the aneurysm, it can not be relied upon as a means of acquiring the internal geometry of the aneurysm, can not be used in automatic geometric data acquisition, and requires extravascular access thus becoming extremely ill–suited for the purposes of this project.

### 3.2.2 Digital Subtraction Angiography

DSA is a digital implementation of traditional radiographic angiography [Bro84]. It is based on the difference in absorption of X-rays by different anatomical structures and tissues. Absorption is dependent on their mass, chemical composition and projected X-ray energy. The latter is typically a compromise between detector sensitivity which requires sufficient energy to be used in order for the desired signal–to–noise ratio to be achieved and patient safety which requires the energy to be minimized. The intensity of the detected X-rays can be used to determine the nature of the objects that lie in their path. Since blood vessels and blood are non–X-ray–opaque and do not register on an X-ray scan, a radio-opaque dye must be injected inside the vessel in order for it to be seen. Typically, multiple scans are performed while the bolus travels through the region measured by the scanner. In the case of DSA, a digital detector produces a sequence of digital images that shows the distribution of the dye along the vessel.

Figure 3.1 shows a typical lateral projection DSA sequence that starts from an empty aneurysm, shows how the aneurysm gets filled with dye, how dye is flushed out, and terminates with another non-opaque image. Lower intensities represent a higher concentration of dye and all other X-ray–opaque structures such as bones,

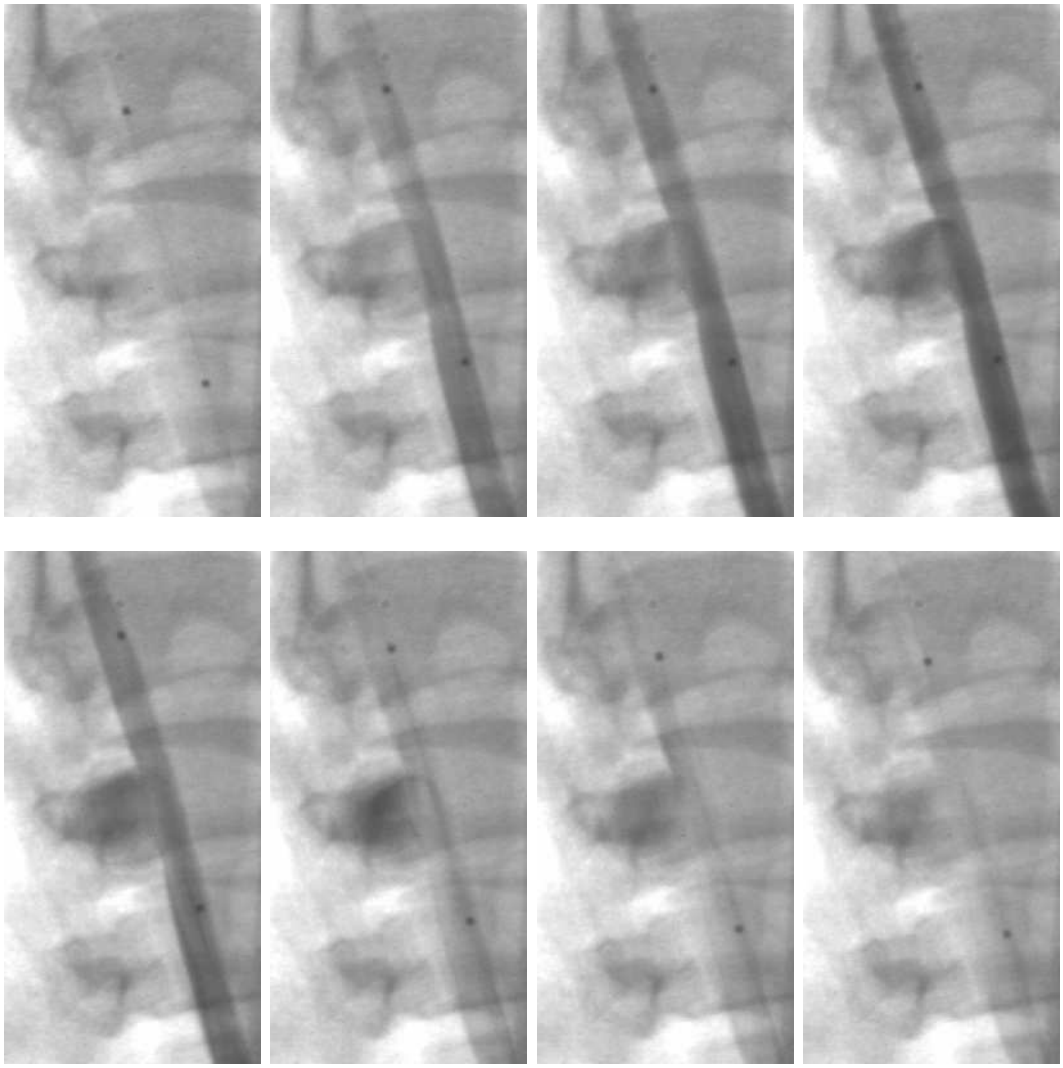

Figure 3.1: A typical sequence of angiographic images of a swine aneurysm, lateral projection.

Figure 3.2: Subtracted lateral angiographic projection of swine aneurysm.

which do not move while the sequence is acquired and thus appear in the same position on all images in the sequence. Subtraction allows to concentrate view on the vessel in question by removing all irrelevant structures from each image in the sequence [Kri95]. Figure 3.2 shows the subtracted image from which the stationary tissues are removed.

Although conventional DSA does not typically generate three-dimensional images, it can produce a number of two-dimensional projections that can be used to estimate the original geometry. The minimal set of projections may include an anteroposterior and a lateral one while extended sets can include as many projections at different angles as necessary to achieve the desired precision. DSA is widely used, fast, inexpensive, and has good spatial resolution, and thus can not be overlooked as a source of geometry data despite its intrusiveness, inherent two–dimensionality and vulnerability to *motion artifacts* which are caused by movement of the patient or vasculature during the acquisition of the DSA

sequence [PHS93].

The imaging technique used in the UCLA Department of Radiological Sciences for the purpose of monitoring the position of the catheter during brain aneurysm surgery is DSA [GJM94]. All other imaging techniques reviewed in this thesis are currently incapable of producing real–time information of catheter movement.

### 3.2.3 Magnetic Resonance Imaging and Angiography

Magnetic Resonance Imaging (MRI) is based on the different magnetization characteristics of different tissues when exposed to a strong magnetic field [Spr93]. The characteristics used as the source of contrast are proton density and magnetic relaxation times T1 and T2 (longitunal and transversal relaxation times respectively). In order to perform an MR scan, a patient's body is placed in a strong magnetic field that changes the magnetization of the tissues and causes them to resonate at specific frequencies in the radio frequency (RF) range. Different tissues generate their peak resonation response at different frequencies, achieve different levels of magnetization, and change their magnetization at different rates.

Magnetic Resonance Angiography (MRA) is a variation of magnetic resonance Imaging (MRI) that uses nuclear magnetic resonance to detect motion or flow [PHS93]. It is also useful in depicting the vessel in which the flow occurs, but the MRA representation of the vessel is more *functional* than *anatomical* since it reflects blood flow patterns and velocities [AET93]. The major MRA techniques in current use are time-of-flight (TOF), phase-contrast (PC) and long T echo (TE), the first and the second of which both have two- and three-dimensional versions. The mentioned methods can be described as:

1. **Sequential 2-D TOF MRA** depicts the protons that enter a designated volume (a thin slice or slab within the patient). In an image, the inflowing blood is bright while tissue and the blood that resides in the volume stay dark. As the result of RF pulses the magnetization of stationary tissue and blood is suppressed (saturated) from lining up with the magnetization of the external magnetic field. The relaxed (co-aligned with the external magnetic field) inflowing blood enters the saturated volume and starts changing its magnetization. The initial magnetization and the rate of change of magnetization in both the longitunal and transversal directions are used to depict the inflowing blood. In order to cover a given volume, when one slice is acquired, the position of the acquisition volume is shifted slightly and the next slice is acquired. The resolution can be enhanced by overlapping the neighboring slices. This method is more sensitive to slow-moving blood than its 3-D version but still has a lower bound on acceptable flow speeds.

2. **3-D TOF MRA** is similar to the previous method but the whole desired volume (typically 3 to 8 cm in thickness) is acquired at once. Blood must travel fast enough to traverse the slab before it gets saturated and loses contrast but very high resolutions (1 mm and better vs. 1.5 mm) can be achieved. In addition, the volume being imaged does not have to be aligned perpendicular to the flow being recorded, as opposed to 2-D TOF MRA where a flow lying inside the imaged slice would consist of saturated blood and therefore will not be detected. The minimal flow rate restriction can be improved by conducting multiple 3-D TOF studies on thin overlapping slabs but such techniques are time-consuming. Neither of the two TOF methods is capable of countering the signal loss caused by flow turbulence.

3. **2-D Slab PC MRA** computes flow velocity using the difference in spin phase between successive acquisitions. The differences are computed, eliminating the signal from the stationary tissue in process, assigned pixel intensity and displayed or stored. The blood magnetic moment phase shifts are caused when the blood moves along a magnetic field gradient and their numerical value is directly proportional to the flow rate. That requires using multiple orthogonal optimal-flow directions in order to provide a total flow image in complicated non-straight anatomy vessels. One slab acquisition is relatively fast and generates a projection through the volume of interest thus overly thick slabs may result in a loss of contrast.

4. **2-D Cine PC MRA** is a variation of the previous method designed especially for pulsatile flows. Images are obtained at different points in the cardiac cycle and acquisition time is gated to provide synchronization.

5. **3-D PC MRA** is a volume-based PC technique. It allows voxels much smaller than any 2-D PC technique, to segment and project any vascular structure inside the acquired volume and to create directional flow images. Since a scan takes a long time, velocities and flow rates are averaged over many cardiac cycles thus eliminating any possibility to compute the flow profile.

6. **long TE MRA** was developed to facilitate imaging of arterial blood flow and is based on the high transversal relaxation time of oxygenated blood.

Unfortunately, promising techniques such as PC MRA are not widely available, and present more of a topic for future research and implementation than a clinically ready imaging modality.

### 3.2.4 Computed Tomography

This technique produces three-dimensional information on the internal structure of an object from a set of X-ray images of the object obtained at different angles [KS79]. The technique is more widely used than MRI but has numerous drawbacks such as being more harmful to the patient's health than MRI, having worse spatial resolution [See94] and being limited to imaging of axial sections. Effectively, CT presents a less powerful and less expensive alternative to MRI and thus can be considered as an auxiliary mean of aneurysm geometry determination.

A recently developed CT technique known as spiral scanning was found to be promising in detection of intracranial aneurysms [RDS95]. By acquiring whole vascular territories in less than 30 seconds, spiral CT has allowed for CT angiography (CTA), quicker, less expensive and more efficient than conventional DSA. When compared with other forms of angiography, CTA lacks the spatial resolution of both DSA and MRA, and requires injection of a much larger volume of contrast than DSA. On the other hand, it is faster than either DSA or MRA, allows for acquisition of larger number of voxels than the typical MRA scanner, is less susceptible to complex flow dynamics than MRA (as CTA directly images intravenous contrast) [RDS95] and does not suffer from flow aliasing problems known to affect PC MRA [PHS93]. In addition, CT is the only imaging modality available for imaging of patients with metallic implants that can not be safely imaged using NMR.

### 3.2.5 Conclusions

The medical imaging modalities that were found to be useful for the purposes of determining the internal geometry of the parent artery–aneurysm complex can

be divided into two classes:

- **Tomographic methods** where multiple 2-D projection images of the studied object are taken at different angles and the resulting 3-D volume image is computed using filtered back projection or convolutions [KS79]. These techniques have been used widely in CT and MRI [Spr93] but may not be best suited for determining the geometry of a blood vessel: CT may need dye to be injected into the vessel while MRI might have problems with recognizing the vessel walls from other tissues.

- **MRA methods** including TOF and PC MRA. The former records both the flow inside the vessel and the tissue of its walls [AET93]. 2-D TOF is preferable to the 3-D version because of higher acquisition speed, lower bounds on minimal recordable flow velocity, and better signal–to–noise ratio [PHS93]. However, 2–D TOF MRA requires that the imaging slices be aligned perpendicular to the main flow direction.

Potchen et al. compared MRA and DSA for the purpose of aneurysm detection [PHS93]. They noted that while MRA is non–intrusive, does not require catheterization, produces a 3–D data set and may provide shorter procedure times, it suffers from lower spatial resolution and signal losses from complex flow which may result in a severe underestimation of the size of the aneurysm's neck. While spatial MR resolution can be improved, any improvements tend to require longer acquisition times. In addition, 2–D PC MRA is the only angiography modality that can record aneurysmal wall movement during the cardiac cycle. Another major disadvantage of MRA is high cost and consequently low availability of high-resolution scanners. On the other hand, CT suffers from long

acquisition times, dependence upon bolus injection, and uneven distribution of contrast across the vessel (heavy contrast tends to concentrate in the bottom of the vessel). Yucel [YK94] found CT to be comparable to MRI in aneurysm detection and inferior to MRA.

Naidich and Righi [NR95] found that a complete investigation of an aneurysm may require that both TOF and PC MRA be performed. They also found that the two MRA techniques were comparably efficient on aneurysms sized between 2 and 15 $mm$, while TOF MRA proved to superior with aneurysm sized in excess of 15 $mm$.

Based upon the survey above, 2–D TOF MRA was selected as the primary means of geometric data acquisition. In addition, spiral CTA was selected as the secondary source of geometric information, used either to support MRA data or to replace MRA if it is unavailable or unsafe.

## 3.3 Measurement of Arterial Blood Flow

Both the task of constructing the aneurysm model and the validation task require sufficient knowledge about the flow inside the artery and the aneurysm. For the former task a description of artery blood flow towards the aneurysm will suffice while for the latter one the flow must be measured in multiple points. Historically, early flow measurements methods were based on measuring the amount of injected indicator and the average arterial concentration of the indicator (also known as indicator dilution methods) [Cha82]. Blood flow measurements typically employ one of the following techniques: electromagnetic, ultrasonic flow meters, laser Doppler anemometry or magnetic resonance-based flow measurement (a description was given in Section 3.2.3).

An alternative approach is based on determining local or instantaneous flow by analyzing digital images obtained by digital subtraction angiography or otherwise.

### 3.3.1 Electromagnetic Flow Meters

These meters essentially record the electrical currents induced by a flow of electrically conductive blood through a vessel aligned across a magnetic field. In the simplest case, where the magnetic field is uniform and the vessel has constant diameter and shape all over its length, the recorded response is a linear function of the flow velocity [Max82]. More complicated cases (non-straight or variable-diameter blood vessels) require exact knowledge of the vessel's geometry in order to calculate the flow velocity from the recorded current. It was noted in [Kri95] that while such methods are convenient for phantom experiments their use *in vivo* requires that the blood vessel be exposed, which is impractical if the vessel is seated deep.

### 3.3.2 Ultrasonic Flow Meters

Most ultrasonic flow meters are based on one of two basic principles:

1. **Time of transit** – the flow velocity is calculated using the difference of ultrasonic beam transit times in the original and opposite directions.

2. **Doppler methods** – the flow velocity is calculated using the differences in frequency of the ultrasonic returned echoes backscattered from the blood cells.

Both techniques allow for either intravascular or extravascular measurements, the former by inserting transducers assembled inside a catheter tip into an artery and

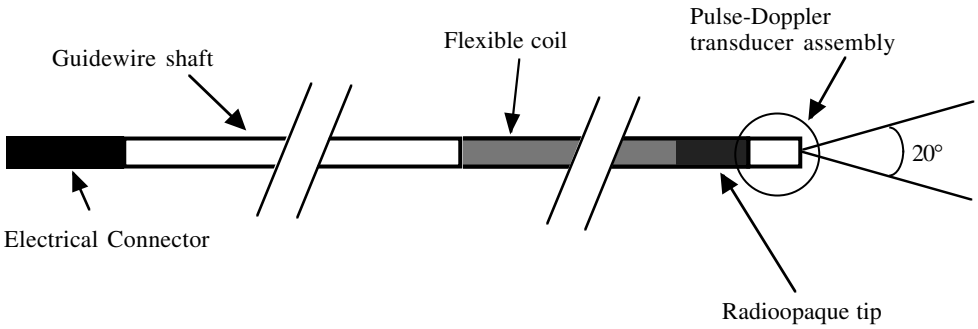


Figure 3.3: Diagram of the *Cardiometrics* Doppler guide wire.

the latter by using external receiving/transmitting equipment. The latter method has the advantage of not disturbing the flow but its use is limited to open-chest procedures. The measurements used in this thesis for validation purposes were conducted by an intravascular pulsed Doppler probe connected to a *Cardiometrics Model 5500* ultrasonic flow meter.

Following its description in [DCP92] we will note that the probe as seen in Figure 3.3 is connected to a 175–cm–long 0.018–$in.$–diameter flexible and steerable guide wire. The probe itself is based on a piezoelectric ultrasound transducer that emits an ultrasonic beam diverging $\pm 10$ degrees from the probe's axis, the sample volume being 0.65 mm thick by 1.7 mm in diameter located about $5mm$ beyond the guide wire tip. The probe averages the flow velocity component that is parallel to the probe inside the sample volume as seen in Figure 3.4 where the sample volume is designated by a shaded rectangle, its aperture by $\alpha$ and the angle of incidence of the probe with the flow direction by $\theta$.

*Cardiometrics* also supplied other probes which differed from the one described above by the transducer aperture (up to $\pm 12.5$ degrees) and sample vol-

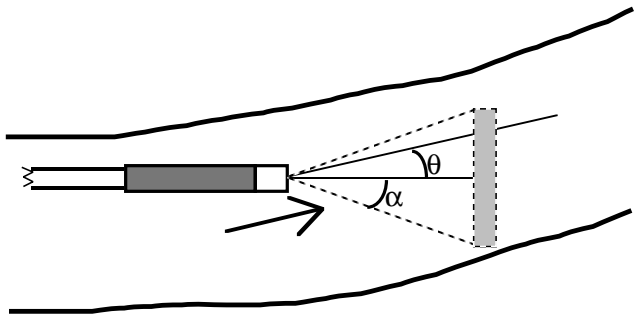


Figure 3.4: Doppler probe and angles of incidence.

ume diameter [Kri95]. The probe measures the time average of the instantaneous spectral peak velocity (APV), maximum and minimum spectral peak velocities (SPV), and spectral pulsatility index (SPI).

$$SPI = \frac{maxSPV - minSPV}{APV}$$

The results are recorded to a velocity strip chart similar to the one seen in Figure 3.5. Assuming a time-averaged parabolic velocity profile across the vessel, the mean flow can be estimated as [DCP92]

$$Q_D = \frac{\pi D^2}{4} \cdot \frac{APV}{2} \tag{3.1}$$

where $Q_D$ is the Doppler-derived time-average flow, $D$ is vessel internal diameter at the location of the sample volume ( 5 mm distal to the probe tip ) and $APV$ is the time average of the spectral peak velocity.

It is important to note that Doppler imaging has the inherent disadvantage that the Doppler frequency shift depends upon the angle between the ultrasound beam and the direction of flow. The shift achieves its maximum when the beam and flow are co-aligned; it decreases with decreasing incidence angle, and drops to

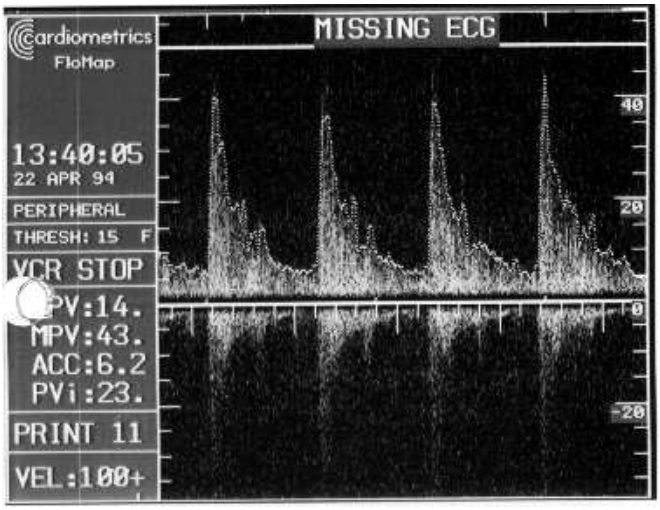


Figure 3.5: An example of intravascular Doppler measurements.

zero when the flow is perpendicular to the measuring beam [Spr93]. Effectively, the meter measures the component of flow velocity aligned with the beam:

$$v_{doppler} = cos(\theta) \cdot v_{real}$$

where $v_{doppler}$ is the measured velocity, $v_{real}$ - the real velocity and $\theta$ - the angle of incidence. Despite this shortcoming, the meter was proven [CVK94] to produce good measurements of the blood flow under various flow conditions.

### 3.3.3 Videodensitometric Techniques

The determination of blood flow characteristics via non–invasive imaging is highly desired since it is significantly easier than intrusive methods, does not require the involvement of a surgeon, does not disturb the flow in any way, and can be performed on an analysis workstation. Also, as DSA already sees wide clinical usage for the purpose of obtaining high–quality blood vessel images, it is advantageous

to use these images to produce quantitative flow data [SHC89].

The complexity of the task of videodensitometric flow quantitation is due to the fact that the vessels are typically asymmetric and twisted while the flow is pulsatile, has non-uniform non-zero radial velocity, may be complicated by turbulence or flow separation effects and radial velocity might not be much lower than the axial velocity. This complexity causes all techniques existing in mid-1990s to make numerous assumptions about the nature of the flow and the shape of the vessel that may reduce their field of applicability to phantoms or very narrow classes of blood vessels. None of these techniques is well-suited for measurement of blood flow inside an aneurysm. Generally, all techniques can be divided in three major classes:

- time-of-transit methods,
- distance-density methods and
- conservation methods.

#### 3.3.3.1 Time-of-Transit Methods

Methods belonging to this group tend to be less complicated than other techniques and thus have been investigated more widely. They are based on employing time–density curves that plot the density of bolus in a given Region of Interest (ROI) vs. time of acquisition. The density is typically averaged over the area of an ROI [Kri95]. Two typical time–density curves are shown in Figure 3.6, where the first ROI is located upstream of the second one and demonstrates lower bolus dispersion over time.

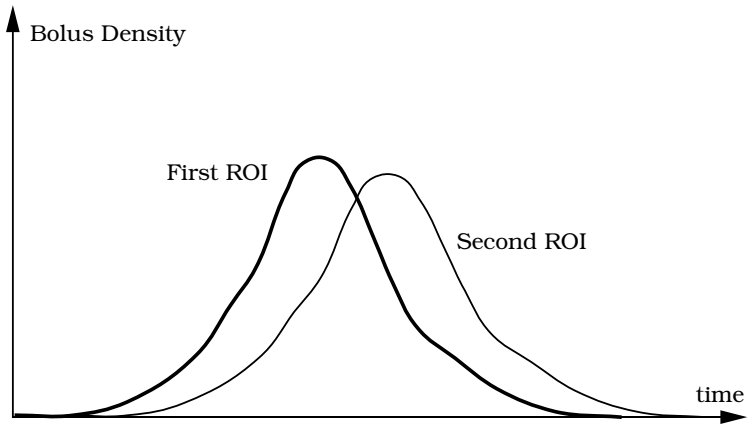


Figure 3.6: An example of time–density curves for two ROIs.

Flow velocity can be calculated as:

$$v = \frac{\Delta x}{\Delta t} \tag{3.2}$$

where $\Delta x$ is the distance between the two ROI and $\Delta t$ is the time it takes the bolus to travel between the two ROIs, which can be computed as $\Delta t = (t_2 - t_1)$ where $t_1$ and $t_2$ represent the time of bolus arrival at first and second ROI respectively.

Problems inherent to this class of methods include hardship of accounting for the pulsatile nature of blood flow and non-uniform shape of the vessel [CHB86].

The question of determination of the bolus time of arrival at an ROI has been investigated widely. Among the most popular methods are the following ones:

1. **Time of peak amplitude** - the bolus is considered to arrive when the peak of time-density curve arrives, as shown in Figure 3.7.

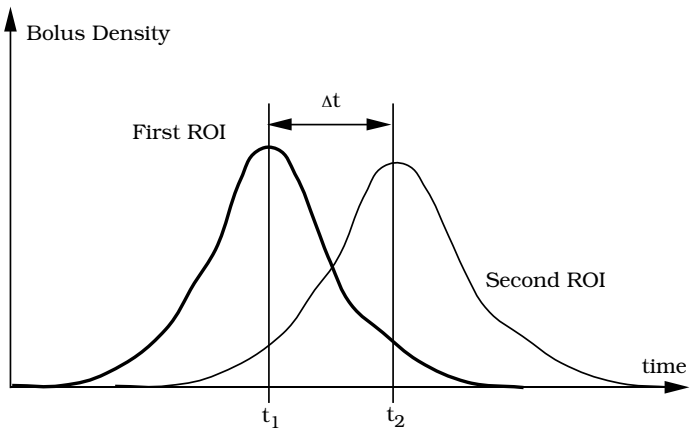


Figure 3.7: Time–density curves. Time of peak amplitude.

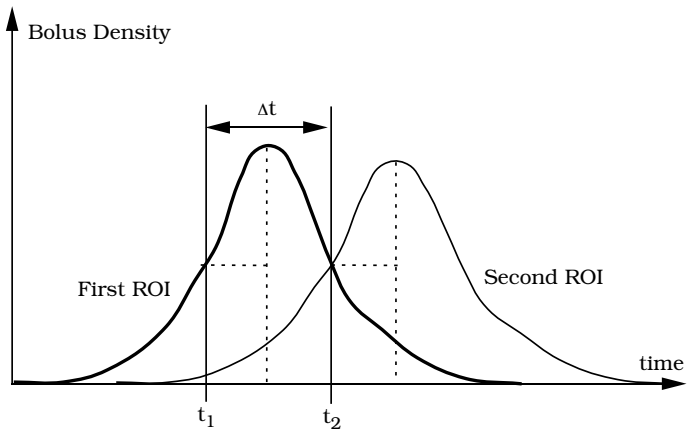


Figure 3.8: Time–density curves. Time of half–peak amplitude.

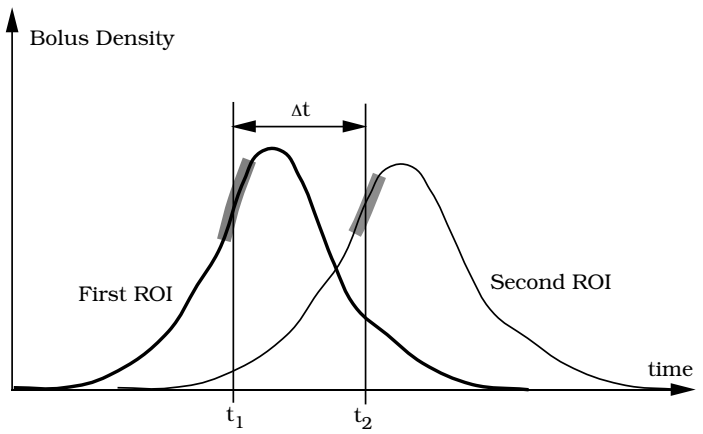


Figure 3.9: Time-density curves. Time of peak gradient.

2. **Time of half-peak amplitude** - the bolus is considered to arrive when the first (i.e. located before the total peak) half-peak of time-density curve arrives, as shown in Figure 3.8.

3. **Time of peak gradient** - the bolus is considered to arrive when the gradient of the time-density curve achieves its maximal value, as shown in Figure 3.9.

4. **Mean concentration time** - the time-density curve is integrated over time from zero time to the peak time and divided by the peak density value. The resulting mean concentration is subtracted from the time-to-peak.

5. **Leading edge** - the bolus is considered to arrive when the arrival of the leading edge is detected [FHS79].

None of these methods are suited for recovering a flow velocity profile and

none of them are well-suited for computing even average velocity of pulsatile flows since averages tend not to be computed over an integer number of cardiac cycles and thus either over- or under-estimate the average velocity because the numbers of peaks and anti-peaks would not be equal. The problem can be solved either by averaging the velocity over a large number of cardiac cycles so that the effect of one partial cycle would not be significant or by correcting an estimate obtained by one of the methods listed above.

Research in our group [Kri95] described a technique based on a multiplicative correction factor. Under this approach, the real velocity can be calculated as

$$v_{real} = C \cdot v_{btt} \tag{3.3}$$

where $v_{btt}$ is the average velocity computed using the measured bolus transport time and $C$ is the correction factor which can be computed as

$$C = \frac{(R+3) \cdot (T_2 - T_1)}{(1-R) \cdot [(T_2^4 - T_1^4) - 4(T_2^3 - T_1^3) + 6(T_2^2 - T_1^2)] + 4R(T_2 - T_1)} \tag{3.4}$$

where $R$ is the ratio of maximal to minimal velocity while $T_1$ and $T_2$ are ratios of time when the measurements were started or stopped to the cardiac cycle length (when the measurements are done over the whole cycle length, $T_1 = 0$ and $T_2 = 1$).

Generally, such correction techniques are based on fitting the measured data to some standard cardiac cycle with known and constant length and flow velocity shape. While such an approach may be useful in a laboratory experiment where the cardiac cycle and the flow can be effectively controlled, any variation in the cycle duration or the velocity shape will require all variables in the correction factor to be recalculated and another standard cardiac cycle to be established.

As concerning the improvement of time–of–transit methods by averaging the

velocities obtained on a large number of cardiac cycles, we must note that obtaining a sequence of still images needed for such averaging can not be done without either performing an extremely long injection or a large number of short injections which may not be feasible, especially in the middle of a surgery.

#### 3.3.3.2 Distance-Density Methods

This class of method is based on performing operations on concentration–distance curves such as shifting and matching curves obtained at different moments of time. This method was investigated by Seifalian et al. [SHC89], [SHH91], [HSC94], Hoffman et al.[HD90] and du Boulay et al [dBC86, CHB86].

Following the description in [SHC89], we will define a match between two distance–density profiles as the spatial shift where the sum of the squares of the difference between the two profiles is a minimum. The bolus velocity can be calculated by dividing the obtained shift by the time interval between the profiles.

If we define the concentration of bolus at axial position $x$ and time $t_i$ as $K_{t_i}(x)$ where $t = 0, t_1, ..., t_{max}$ and $x = 0, 1, ..., x_{max}$, the match criteria for the forward–directed flow may be given as:

$$\sum_{x=n}^{x_{max}} \left[K_{t_i}(x-n) - K_{t_{i+j}}(x)\right]^2 \tag{3.5}$$

The value of $n$ that minimizes Equation 3.5 is the distance traveled by the bolus during time $t_{i+j} - t_i$. It is advantageous to match concentration–distance profiles obtained on subsequent time frames (i.e. $j = 1$) since that would minimize the movement of the bolus between profiles and allow us to match more profile points than when using non–adjacent frames. On the other hand, as any other shifting–and–matching method, the distance–density techniques have limits on

the measured velocity imposed by the field of view and temporal and spatial resolution of the acquisition device. In fact, the theoretical maximum velocity that can be calculated using a distance–density method is equal to

$$V_{max} = \frac{(N-1) \cdot a}{\Delta t} \tag{3.6}$$

where $N$ is the number of pixels positioned along the vessel (typically, it is equal to the size of the image), $a$ is the pixel size along the axis of the vessel (typically, it is equal to the pixel size) and $\Delta t$ is the time interval between consecutive frames.

The concentration of bolus $K_{t_i}(x)$ at a given axial position $x$ and time $t_i$ is assumed to be an integral of bolus concentration over a cross-section of the given vessel.

Such techniques assume uniform translation of bolus between successive frames and hence are vulnerable to flow separation or strongly peaked non- uniform radial velocity profiles within a frame. In addition, the frame rate must be sufficiently high to ensure that the bolus does not transit through the region of interest between successive frames.

#### 3.3.3.3 Conservation Methods

Conservation methods present the oldest group of videodensitometric techniques. They are based on using various conservation laws applied either locally or globally, over a time interval or instantaneously.

Their development was started with global mass conservation methods such as the Stewart-Hamilton method [Zie62], which is based on using the relation of the total bolus mass to the time- and cross-sectional integral of the bolus density ( image intensity ) in a vessel. The method produces a mean flow velocity that must

be weighted by the contrast density in order to obtain the instantaneous velocity of a pulsatile flow. Successful application of this method requires the knowledge of total bolus mass and the *DSA system calibration* - the ratio between the DSA signal and line-integrated bolus density.

Methods of the "optical flow" class use a local instantaneous mass conservation law expressed through the continuity equation. The flow is assumed to be incompressible which is reasonable at typical blood flow velocities [SUS94, SYU89].

Research in our group described a method that [CDV92] simultaneously used mass and momentum conservation laws for laminar flow of incompressible fluid resulting in the continuity equation

$$\frac{\partial \mu}{\partial \tau} + \mathbf{v} \cdot \nabla \mu = D \nabla^2 \mu \tag{3.7}$$

and the equation of state

$$\nabla \mathbf{v} = 0 \tag{3.8}$$

where $\mu$ is the bolus density, $\mathbf{v}$ is the flow velocity and $D$ is the diffusion coefficient. Assuming diffusion to be negligible and substituting Equation 3.8 into Equation 3.7 yields the equation of continuity for incompressible flow:

$$\frac{\partial \mu}{\partial \tau} + \nabla \mathbf{v} \mu = 0 \tag{3.9}$$

Assumption of uniformness of the contrast mixing allows to derive 3.9 into

$$\int_{\eta_1}^{\eta_2} \left[ P(\eta, t_2) - P(\eta, t_1) \right] d\eta + \Gamma \int_{t_1}^{t_2} \left[ \frac{P(\eta_2, t)}{A(\eta_2)} - \frac{P(\eta_1, t)}{A(\eta_1)} \right] dt = 0 \tag{3.10}$$

where $\Gamma = Au$ is the flow rate, $u$ is the flow velocity, $\eta$ parameterizes the vessel length, $t$ is time, $P(\eta, t)$ is the integral of contrast density over a vessel cross–section at axial location $\eta$ and time $t$ while $A(\eta)$ is the cross–sectional area at

location $\eta$. Discretizing Equation 3.10 yields

$$\sum_{\eta=\eta_1}^{\eta_2} [P(\eta, t_2) - P(\eta, t_1)] + \Gamma \sum_{t=t_1}^{t_2} \left[ \frac{P(\eta_2, t)}{A(\eta_2)} - \frac{P(\eta_1, t)}{A(\eta_1)} \right] = 0 \tag{3.11}$$

Solving 3.11 for $\Gamma$ we obtain

$$\Gamma_{t_2,t_1,\eta_2,\eta_1} = \frac{\sum_{t=t_1}^{t_2} \left[ \frac{P(\eta_2,t)}{A(\eta_2)} - \frac{P(\eta_1,t)}{A(\eta_1)} \right]}{\sum_{\eta=\eta_1}^{\eta_2} [P(\eta, t_2) - P(\eta, t_1)]} \tag{3.12}$$

which is the formula for flow rate obtained on time-spatial interval $[t_1, t_2] \times [\eta_1, \eta_2]$. It was noted that reduction of statistical noise can be achieved by calculating $\Gamma$ on multiple small overlapping elements with increasing axial length using space- and time-integrated segment density as the statistical weighting factor. Both $\Gamma$ and its associated uncertainty can be calculated using the method of least squares.

The method does not require high frame rates (in fact, it was validated using acquisition rates of 5 to 6 frames per second while recording flows with velocities up to 76 cm/sec) necessary for distance-density methods, however, higher frame rates may provide for improved accuracy. On the other hand, since either the frame rate or the field of view can be reduced in comparison with the requirements of the distance-density methods, the total X-ray exposure of the patient can be reduced significantly.

### 3.3.4 Conclusions

Since using extravascular flow measurement tools to determine blood flow velocity in brain arteries defeats the purpose of purely endovascular aneurysm treatment, our means of flow measurement are limited to the use of intravascular ultrasonic flow meters and the use of videodensitometric techniques. While accurate intravascular ultrasonic flow meters tend to be expensive, scarcely available and require an additional microcatheter to be operated inside the parent artery,

videodensitometric methods of instantaneous flow measurement do not require anything except for a DSA scanner, already employed by neurosurgeons to monitor the progress of their microcatheters.

On the other hand, intravascular ultrasonic flow meters have been validated and proven as efficient tools for potential endovascular applications, while videodensitometry has yet to be proven to be clinically useful and is still a research topic.

Taking into consideration the issues of cost, availability and accuracy, we will employ intravascular ultrasonic flow velocimetry as the primary mean of flow measurement for the purposes of constructing physiologic models in this thesis. We will also note that videodensitometric techniques are a promising way of measuring brain blood flow and therefore should be investigated more closely.

## 3.4 Geometric Modeling

All aneurysm model construction methods can be divided into two major classes: manual and automatic construction. As much as automatic model generation is desired for the project, manual generation can be used for simulation validation purposes as a temporary solution. In addition, the generation strategy depends heavily upon the requirements of the computational fluid dynamics (CFD) software used: as an example, some packages require a hexahedral mesh to be developed and typed in, other require an irregular tetrahedral mesh, etc. Therefore we will review the model requirements of the CFD packages employed to perform the simulations: *Fluent/UNS* (Fluent Inc., Lebanon, N.H.) and *NEKTON* (also Fluent Inc., Lebanon, N.H.). Typically, such requirements impose a low bound on grid quality as different CFD solvers may be more or less vulnerable to low

grid quality.

### 3.4.1 Requirements Imposed on Geometric Models by *NEKTON*

*NEKTON* can be described as a previous-generation CFD package. It uses a spatial discretization based on the spectral element method (SEM), a high-order derivative of the finite element method. Such discretization requires the computational domain to be divided into a set of large macro-elements inside which the geometry is precisely approximated by higher-order polynomial expansions. In three-dimensional domains, the macro-elements are hexahedrals each face of which is a non-degenerate quadrangle. The *NEKTON* pre-processor, *PreNEK* generates hexahedra using two quadrangles which represent the "top" and "bottom" faces of the element. The other four faces ("right","left","front" and "rear") are defined by the four surfaces that connect each of the four respective sides of the two quadrangles. Third-party mesh generators do not have to generate hexahedra in this way. Generic spectral element method restrictions prohibit elements from lying inside each other, from having internal angles $\theta \geq 180\,\text{deg}$ and from sharing less than an entire common side or face. An additional restriction imposed by *PreNEK* is that a 3-D mesh must be constructed by adding layers of hexahedral spectral elements in the $z$-direction. The top and bottom faces of the elements must be parallel to the $x$-$y$ plane and the bottom of the first element is located at $z = 0$.

In order to minimize divergence and maximize accuracy, the spectral elements must comply with the following rules:

- interior angles of the spectral elements should lie within $90 \pm 30\,\text{deg}$, angles close to $90\,\text{deg}$ provide for the best accuracy;

- variations in element size should be relatively smooth; changes in size between adjacent elements should be limited by a factor of about 3;

- a sufficient number of spectral elements of sufficiently high order must be provided if the model includes a complicated time-dependent interface such as pulsatile flow; an underresolved geometry will result in a wiggled solution [Flu92].

### 3.4.2 Requirements Imposed on Geometric Models by *Fluent/UNS*

*Fluent/UNS* is a CFD package which can use spatial discretization based on both unstructured tetrahedral grids and structured or unstructured hexahedral grids [Flu94a]. Although structured grids were found to be the most commonly used for CFD purposes, unstructured grids tend to be used more and more widely as they are inherently more flexible for complex geometries and grid enhancement than the structured ones. Unstructured grids also provide for reduced computational time and improved accuracy [WNM94]. Some CFD packages also can perform *mesh adaptation* - modification of the grid in order to better resolve the features in the flowfield during the solution process.

The developer of *Fluent/UNS* imposed the following requirements on its input grid:

- the overall number of nodes should be sufficient to resolve all flow features (boundary layers, separated regions, mixing zones etc.) using at least $3-4$ nodes per flow passage;

- element aspect ratio requirement – generally, ratios in excess of $5:1$ should be avoided unless the gradients in one direction are very small relative to

those in the others;

- grid skewness – excessively skewed grids should be avoided, element faces should be close to equilateral;

- rate of element size change in non-uniform grids – the size of adjacent elements should not change by more than 50%;

- grid spacing near walls - should be small enough to ensure accuracy of calculations, especially for laminar flows [Flu94a].

Unfortunately, both *NEKTON* and *Fluent/UNS* user manuals provide almost no numerical measures of grid quality. However, this question has been investigated by other researchers. Their results will be presented in the following subsection.

Tetrahedral/triangular grid generator *TGrid* (Fluent Inc., Lebanon, N.H.) can be used as a source of quality meshes for *Fluent/UNS* using Delaunay triangulation with discretized boundary meshes (nodes and triangular faces in the 3–D case) as its input.

The generator uses a two–stage process including generation of a so–called initial boundary mesh and insertion of internal nodes to cover the whole volume of the object. In process of creation and refinement of the internal grid, the two controlled quality measures are element volume (must be below some user-supplied upper bound) and cell skewness $\xi$ defined as

$$\xi = \frac{S_{optimal} - S_{cell}}{S_{optimal}}$$

where $S_{cell}$ is the cell size and $S_{optimal}$ is the size of an equilateral cell with the same circumsphere radius as the cell under consideration [Flu94b]. Grid cells with

$\xi < 0.25$ are considered excellent, with $0.25 < \xi < 0.5$ good, with $0.5 < \xi < 0.75$ fair, with $0.75 < \xi < 0.9$ poor and with $\xi \geq 0.9$ bad or degenerate.

The generator developer defined quality 3–D grids as ones having the average skewness value of approximately 0.4 or lower, having no boundary (2–D) cell with skewness worse than good ($\xi \leq 0.5$) and having most internal cells good with a limited number of fair and, possibly, a few poor cells.

The quality of input boundary mesh is measured by clustering, smoothness and skewness. Appropriate clustering ensures adequate resolution of the features of the solution field, where higher density of grid points is necessary in regions with complex geometry or high expected solution gradients (the latter requirement can be somewhat relaxed if the CFD solver provides solution–dependent mesh refinement). The accuracy of the approximations used in most CFD solvers depends upon the assumption of smooth variation in cell sizes and suffers if it fluctuates rapidly. Similarly, highly skewed elements result in high truncation errors and inefficient use of memory and computational time.

### 3.4.3 Numerical Measures of Tetrahedral Grid Quality

Weatherill et al [WNM94] introduce two numerical measures of unstructured tetrahedral grid quality:

$$\omega = \frac{Radius\ of\ circumscribed\ sphere}{Maximum\ edge\ length}$$

and

$$\zeta = \frac{Maximum\ edge\ length}{Minimum\ edge\ length}$$

These measures allow three cases of unacceptably bad tetrahedra to be defined:

- $\omega = O(1), \zeta \gg 1$ : needle–like tetrahedra with one acute solid angle and very low area of the opposing face,
- $\omega \gg 1$ : flat tetrahedron, and
- $\omega = O(1), \zeta = O(1)$ : tetrahedron is a sliver with all edges of similar length.

Additional measures of grid quality may include

- $\beta = \frac{Radius\ of\ circumscribed\ sphere}{Radius\ of\ inscribed\ sphere}$,
- $\sigma = \frac{Maximum\ edge\ length}{Radius\ of\ inscribed\ sphere}$,
- $\alpha = \frac{(Average\ element\ edge\ length)^3}{Volume}$,
- $\gamma = \frac{(R.M.S.\ edge\ length)^3}{Volume}$, and
- $K = \frac{(Volume)^3}{(Summation\ of\ all\ surface\ area\ of\ triangle\ faces)^2}$.

The optimal values for the measures are obtained on an equilateral tetrahedron and are equal to $\alpha_{equilateral} = 8.479$, $\beta_{equilateral} = 3.0$, $\gamma_{equilateral} = 8.479$, $\sigma_{equilateral} = 4.8989$, $\zeta_{equilateral} = 1.0$, $\omega_{equilateral} = 0.6125$ and $K_{equilateral} = 4.5 \cdot 10^{-4}$. It was mentioned that $\alpha$ is very successful in identifying elements with volume degenerating to zero.

Although no criteria of grid smoothness was introduced, a Laplacian-based numerical method of smoothness enhancement was provided. Overall grid quality enhancement was described as an iterative process involving the removal of a class of elements with high values of distortion parameter $\alpha$.

Dannenhoffer et al [DW94] provided the following grid quality measures for both structured and unstructured grids:

1. ratio of minimum–to–maximum side lengths in an element,
2. ratio of minimum–to–maximum adjacent volumes,
3. minimum normalized dihedral ( included ) element angle,
4. ratio of cube of average edge length to the element volume,
5. ratio of cube of RMS edge length to the element volume,
6. ratio of minimum–to–maximum side length for a node,
7. number of edges connected to a node (specific to unstructured grids),
8. number of elements connected to a node (specific to unstructured grids),
9. ratio of minimum–to–maximum diagonal lengths (specific to structured grids), and
10. ratio of minimum–to–maximum areas of opposing faces (specific to structured grids).

Among them, measures (1),(3),(4),(5),(9), and (10) measure element quality while (2),(6),(7) and (8) measure the quality of transition between elements and thus grid smoothness. One may notice that the mesh requirements imposed by *NEKTON* in the previous subsection ensure maximization of some of the grid quality measures given above.

## 3.5 Physiologic Modeling

For the purposes of this study, a physiologic model can be considered to be a tempo–spatial flow field, i.e. a description of blood flow as a function of time

in different locations. Considering the different purposes of the two physiologic models that are needed to be created (the model of blood flow in the intake of the parent vessel–aneurysm complex and the model of blood flow through the aneurysm and the parent vessel), two different sets of requirements must be considered.

Of the two models listed above, the former is required by CFD software in order to perform simulations and the requirements on it, if any, are imposed by the design of the CFD solvers. The latter model is needed for validation studies and the requirements on it are imposed be the selected validation procedure.

### 3.5.1 Requirements Imposed by CFD Packages

The CFD software packages used to perform simulation require physiologic models in form of subroutines written in high–level programming languages (FORTRAN for *NEKTON* [Flu92] and C for *Fluent/UNS* [Flu94a]). Such subroutines return velocity components in a given (by coordinates) position at a given time. Both time and position coordinates are supplied to the subroutine as parameters [Flu96, Flu92]. The subroutines are compiled together with the CFD package code and are called by it during its execution.

### 3.5.2 Requirements Imposed by the Validation Procedure

Such requirements are much more lenient than the ones imposed by CFD software. It was decided to store flow velocity measurements as functions of time with the information on location and orientation of the probe attached.

# CHAPTER 4

# Image Processing

Image processing is widely used to change appearance of images in order to facilitate viewing and measurement of their features. As both geometric and physiologic modeling procedures use images of various kinds as the sources of information, the use of image processing may prove to be beneficial for the purposes of this thesis. Numerous image processing techniques have been described in literature and implemented in existing software packages.

## 4.1 Introduction

A need for the following two classes of image processing techniques is seen:

- Image enhancement for preconditioning the data, and
- Segmentation for extracting the boundary of the vasculature and the shape of the aneurysm from the image.

The former is necessary to improve the quality of medical images containing both geometric and physiologic information about the studied aneurysm before any other kind of processing is done. Such enhancement may be provided by some advanced models of acquisition equipment but the set of available techniques may be small and enhancement may be ill–tuned for our purposes, causing loss

of important information. The latter is necessary to separate the parent artery–aneurysm complex from other objects present in the image.

## 4.2 Image Enhancement Techniques

Many images contain defects due to imperfect acquisition devices, inadequate or non–uniform illumination at the moment of acquisition or an undesirable acquisition viewpoint. The problem of correcting such defects in a digitized image has been extensively researched and many solution methods have been developed [Rus95]. While these methods are incapable of achieving the quality levels demonstrated by optimized acquisition procedures or improved detectors, they still present a relatively cheap and powerful way of making up for any acquisition shortcomings, especially since some of them may be unavoidable.

The list of possible image defects includes:

- Noise,
- Blur due to object motion,
- Detector defects, and
- Light spots.

Russ [Rus95] discusses in great detail such image enhancement methods as neighborhood averaging and other kernel-based neighborhood smoothing methods, contrast expansion and manipulation, fractal–based analysis and frequency domain–based filtering.

## 4.3 Segmentation Techniques

Segmentation is an operation which seeks to divide an image into objects of interest [Rus95]. Segmentation may be performed either to find all present objects of interest [Jah93] or to determine the position and shape of an object of interest given by, for example, coordinates of one of its pixels. An image can contain multiple objects of interest (OOI) that are mutually exclusive, uniform and homogeneous with respect to some image property [HS94]. The segmentation operator is defined on given gray scale or color images and produces a binary image where a pixel (or voxel in case of multi-dimensional images) has the value of one if it belongs to the object of interest (OOI) and of zero otherwise.

Some segmentation methods developed in mid–1990s tend to "retain the fuzzy nature of the computation until the highest level possible" [MPL93]. Instead of the binary "object affiliation" image such methods produce a non-binary field where each pixel is assigned the probability of it belonging to the object of interest. While increasing computational load, such methods reduce the information loss for, for example, points close to the boundary. The binary "object affiliation" field can be considered a special case of a probability field with only integer probability values allowed. The fuzzy probability field can be converted into a binary one by thresholding at any moment of time, but this step should be postponed as long as possible due to the associated loss of information.

While detailed descriptions of segmentation techniques are beyond the scope of this thesis, a brief survey of them follows.

### 4.3.1 Basic Segmentation Methods

The most basic segmentation method is thresholding, based upon selecting all pixels within a given brightness range as belonging to the object of interest and rejecting all other pixels. The brightness range is pre–set using *a priori* knowledge, chosen interactively by an operator, or is derived from a brightness histogram [Rus95]. In its basic form, thresholding is highly ineffective on complicated objects or images with defects. Numerous attempts to improve thresholding have been undertaken, resulting in the development of such techniques as multiple-threshold segmentation, variable thresholding, and application of different thresholds in different areas. A survey of thresholding techniques was provided by Sahoo et al. [SSW88].

Subtraction is a method for segmentation of moving objects, applied to a sequence of images obtained at different moments of time. Stationary objects appear in the same locations on all images belonging to a sequence, and therefore can be subtracted out of them, leaving only the moving objects. While subtraction is vulnerable to moving artifacts and is known to reduce signal–to–noise ratio, it provides a powerful yet simple way of segmenting moving objects. Digital subtraction angiography (Section 3.2.2) employs subtraction to obtain a contrasted view of the blood vessel being imaged. While the typical choice of subtraction mask involves either the first frame of the sequence or a roadmap (the least intensive value of each pixel through all frames of the sequence), more complex mask construction strategies allow to improve the quality of segmentation of such objects as aneurysm necks [LTS92]. Various subtraction techniques are surveyed by van Kriekinge [Kri95] and Brody [Bro84].

### 4.3.2 Advanced Segmentation Methods

Numerous drawbacks of thresholding and subtraction have caused the development of more complicated segmentation techniques.

Vincent and Dougherty [VD94] describe a number of segmentation techniques based on the use of morphological operators. Such methods include skeletonizing (computing the medial axis of objects present in an image), object eroding (thinning) and region growing (connectivity–based segmentation) [HS94].

Udupa [Udu94] described algorithms that compute closed and connected boundaries for binary images of arbitrary dimensionality.

A generalized extension of the skeleton concept (known as object representation using cores, or multiscale medial axis) has been found to be efficient in both segmenting and precisely representing object shapes [MPL93]. In this approach, boundary–sensitive operators of varying scales are applied to an N–dimensional image in order to produce a non–binary characteristic function describing "multiscale boundaryness" of every voxel (the probability of this voxel being a boundary of a given scale), and subsequently calculate non–binary "medialness" (probability of the voxel belonging to the medial axis of a given scale). The resulting N+1–dimensional (N image dimensions and the scale dimension) "medialness" field is searched for N–dimensional ridges, which are used to represent the original image [EGM94]. This technique has been shown to be physiologically plausible and to be close to the mechanism of human vision [BP95].

## 4.4 Off-the-shelf image processing software

The *3DVIEWNIX* software package for 3–D visualization and image processing was developed by the Medical Image Processing Group with the University of Pennsylvania Department of Radiology in 1993–1996. It provides a graphical user interface for a set of 3–D visualization functions with added image editing, interactively–controlled thresholding, manual 2–D segmentation and limited filtering (image enhancement) features [Udu96]. The package uses an extension of the ACR–NEMA 2.0 image file format, which is incompatible with the ones used by the UCLA PACS.

The *Magic* library was designed as a proof–of–concept implementation of the cores segmentation technique. It includes a set of utilities providing image enhancement (filtering, small entity removal), skeletonizing and the calculation of 2–D and 3–D cores [Ebe96]. The library uses a set of image file formats incompatible with the ones used by the UCLA PACS.

The GE Research Workstation (GE RWS) was developed as a 3–D visualization and image processing package prototype by GE Medical Systems (Milwaukee, WI) [GE 96]. In 1997 it was redesigned to be based on the GE Visualization Toolkit *vtk* [Sys97]. The toolkit provides a set of utilities including image enhancement(filtering, morphological filtering) basic segmentation (simple versions of thresholding) and boundary mesh generation [SML96].

## 4.5 Selection of Image Processing Methods and Software

### 4.5.1 Image Enhancement

A drawback of all image enhancement methods is that their application inevitably results in a loss of information. While it may be desired to lose information on, for example, noise and scanner defects, useful information may be destroyed in this process. In most cases, it should be possible to select a sequence of image enhancement operations in way that the losses of the useful information are minimized and the losses of the useless information are maximized. Such a sequence may contain numerous applications of different image enhancement techniques in varying modes. Unfortunately, an image enhancement operation sequence optimal for one image may be deteriorating for an image of an object of a different nature, an image obtained using a different scanning device or a different acquisition regime.

It was decided that the usefulness of any of the image enhancement methods should be established by trials employing large numbers of images of similar objects obtained on similar scanners under similar modes. It was also decided to limit the use of image enhancement operations to subtraction (for DSA images) and small entity removal.

### 4.5.2 Segmentation

Similarly to image enhancement, different types of objects and imaging methods may require the use of different segmentation techniques. More general automatic segmentation methods tend to require extremely long computational time while still needing manual result evaluation [Cli97]. The images used for validation

purposes can be classified as belonging to either of the two groups:

- *xyt* images - sequences of 2–D pictures acquired at different moments of time (DSA). The *xyt* designation refers to the fact that such images have two spatial and one temporal dimension.
- *xyz* images - with all three dimensions being spatial (MR, CT).

As the DSA images acquired for validation purposes tended not to contain any objects except for the aneurysm being imaged and a segment of its parent vessel, it was decided that any segmentation methods more complicated than subtraction were unneeded.

The CT and MR images tended to contain some undesired objects (tissue, other blood vessels, etc.). In addition, the automated hexahedral mesh generation procedure (Section 5.3.2) required that segmentation be done. Thresholding was chosen as the segmentation method for CT and MR images due to the ease of implementation and control.

### 4.5.3 Software

It was decided to avoid using any off–the–shelf 3–D image processing software due to negative experience with the versions of *3DVIEWNIX* and *Magic* software available in 1994–1996.

Angiographic sequences were broken into separate frames and segmented using a 2–D image processing package *ImageMagick* [Cri94]. Image enhancement was performed using either *ImageMagick* or during conversion between image file formats.

# CHAPTER 5

# Validation

## 5.1 Previous Studies

Initial validation studies for the simulation were performed by Harreld [Har93]. They included simulating blood flow through models of increasing complexity and accuracy of geometric representation. The studies were divided into three phases. The first phase included simulating blood flow in two–dimensional aneurysms (circular aneurysms on straight arteries) using a number of grids until an acceptable one was found. The second phase included the implementation of a simple 3–D aneurysm model built as a box adjacent to a square duct. The grid was refined until solution convergence was achieved and different assumptions about the flow were tried. The third phase included finding the optimal meshing strategy that allows high geometric detail in the neck and other areas with expected high flow gradients and low detail elsewhere. After a strategy was developed, a model of an experimental aneurysm was built based upon lateral and anteroposterior DSA images obtained in Leo G. Rigler Center for Radiological Sciences of the UCLA School of Medicine.

Simulation results were compared with previous research and angiographic data.

## 5.2 Validation Procedure

The ultimate measure of simulation validity is a comparison of the results with appropriate experimental data. However, degree of validation depends upon the availability of empirical information (which may be prohibitively complicated or even impossible to gather) and the stated goals of the simulation, including the level of detail required and the maximum allowed difference between the simulated and experimental data. If the physical model being simulated is realistic and easily measurable for all variables and areas of interest with desired precision, the validation process is simple and straightforward. However, in a real world environment at least some of these conditions may not hold. For example, not all variables of interest may be measurable, measurements may not be possible in some temporal or spatial areas of interest and measurement accuracy may be low. In the worst case, the physical model being simulated may be impossible to implement, thus prohibiting any experimental measurements. The resulting spectrum of empirical data availability and precision makes absolute validation unreachable. However, sufficient validation can be achieved by verifying that the results of the simulation match the experimental data or theoretical expectations with the required precision.

The multitude of validation levels demands various validation procedures. For the models well–described by empiric data, validation procedures involve matching the simulated and experimental values and analyzing the difference. In the opposite case, the lack of experimental measurements limits a researcher to comparing numerical results with theoretical expectations, independently validating used models and assumptions, and evaluating the efficiency and usefulness of the simulation.

### 5.2.1 Simulation Goals

In the framework of the overall project as described in Chapter 1 and in [Har96], the flow data provided by the simulation is to be used by a virtual reality visualization tool. Initially, the use of the tool is to be limited to assisting physicians in understanding and visualizing blood flow through intracranial aneurysms [Har96]. Eventually the project will be able to simulate endovascular treatment processes, providing physicians with tools for realistic surgeon training, optimal treatment method selection and outcome prediction.

During the initial stage, simulation results only need to match the flow patterns observed in real aneurysms. On the advanced stages, quantitative data on flow, pressure and wall shear stress should be matched with corresponding experimental information obtained during an endovascular treatment procedure.

### 5.2.2 Available Experimental Results

The experimental measurements available for validation purposes were limited to endovascular Doppler ultrasonic flow velocimetry in various points inside the aneurysm and the parent vessel, and videodensitometric time-of-transit flow measurement based on leading edge tracking. The Doppler probe, as described in Section 3.3.2, measures the flow velocity component co–aligned with it, and averages the measurement inside a considerably large sampling volume. The experience of multiple *in vivo* experiments has demonstrated that the probe is hard to navigate into positions where it is co–aligned with the flow direction and the probe tends to rest on the walls, thus reducing the accuracy and usefulness of its measurements. The leading edge tracking-based time-of-transit videodensitometric flow measurement was found to be limited to providing peak flow velocities on

better–quality angiographic sequences.

All geometric measurements (both the size and shape of the aneurysm) and the exact 3–D positions and orientations of the Doppler probes were limited to the use of 3–D manual reconstructions built from two perpendicular 2–D X–ray projections.

### 5.2.3 Simulation Results

The results of the simulation included the values of velocity (three Cartesian components), pressure and solution divergence printed out at all collocation points (Section 2.3.1.6) within the computational domain at specified moments of time.

### 5.2.4 Procedure Selection

As the model being simulated was considered to be far from being "fully described" , it was decided to combine qualitative and quantitative validation, whenever the latter is possible.

The validation procedure included the following steps:

- solution verification,
- qualitative comparison between the numerical results with theoretical expectations, other numerical simulations and experimental observations, and
- quantitative comparison between the velocity of the simulated flow and the Doppler flow velocimetry data.

Since a quantitative comparison requires that the simulated flow velocity is recorded in exactly the same point where the experimental data were obtained,

the position and the direction of the probe in each measurement point must be determined with high precision. If a 3–D reconstruction from two orthogonal X-ray projections does not provide the desired accuracy, quantitative validation may become complicated and probably inconclusive.

## 5.3 Modeling Procedures

In this Section the procedures used to create geometrical and physiological aneurysm models for validation purposes will be described.

### 5.3.1 Manual Geometric Modeling Procedure

Since manual geometry generation is extremely time–consuming, it is desired to use it only on the initial stages of the validation studies and incrementally automatize the process. On the other hand, the manual process is much more flexible and thus more suited for initial studies.

For *NEKTON* the generation process included the following steps:

1. acquisition of DSA images of the aneurysm in lateral, AP and, possibly, other projections,

2. image conditioning (contrast enhancement) and segmentation using subtraction,

3. manual generation of independent 2–D lateral and AP rectangular projection meshes based upon the lateral and AP projections of the aneurysm in question,

4. manual matching of the two independent meshes into a general 3–D hexa-

hedral mesh, and

5. mesh refinement to improve its quality.

### 5.3.2 Automated Geometric Modeling Procedure

Automatic geometry generation is highly desired as it may radically reduce the time necessary to generate the geometry of an aneurysm. Our current approach to automatic geometry generation is based upon sequences of 2–D cross–sectional scans obtained by means of either 2–D TOF MRA or CT. The model generation algorithm is somewhat similar to the manual geometric model construction algorithm and includes the following steps:

1. Acquisition of an image of the aneurysm using 2-D TOF MRA or CT..
2. Image preconditioning (if necessary) to reduce noise, remove small entities etc.,
3. Segmentation to separate the studied object from other recorded objects,
4. Generation of input data acceptable by the CFD package used: a 3–D tetrahedral mesh for *Fluent/UNS* or a regular hexahedral volume mesh for *NEKTON*.

The problem of providing a 3–D tetrahedral mesh for *Fluent/UNS* can be simplified by using the quality 3–D mesh generator *TGrid* described in Section 3.4.2. In this case, the problem is reduced to generation of a 2–D boundary triangular mesh which is used as the input to *TGrid*.

As irregular tetrahedral meshes are used by the currently used CFD package (*Fluent/UNS*) and are likely to be used by the most powerful CFD solvers in

future, the task of generating a triangular surface mesh becomes of the highest priority. Such mesh generators based on marching cubes algorithm were developed for this project by Nicki Sonpar and Branko Marovic within the UCLA Computer Science and Radiological Sciences Departments [Son97, Mar96]. Steps 2 and 3 are described in more detail in Chapter 4.

### 5.3.3 Physiologic Modeling Procedure

Between the two physiological models that have to be constructed, two following functional tasks can be distinguished:

- quantify arterial blood flow, and
- quantify blood flow inside the aneurysm.

The former problem can be characterized by relatively high velocity and simple structure of blood flow. The latter problem, on the other hand, can be characterized by complicated profiles of low–velocity flow. While the solution of the former problem is essentially straightforward: intravascular Doppler measurements were performed in various places inside the parent artery and cineangiographic sequences were analyzed to derive auxiliary flow information, the solution of the latter problem is more complicated. Efficient Doppler measurements require that the probe be co-aligned with the flow in the sample volume, which is next to impossible considering the complexity of flow dynamics inside the aneurysm, relatively low flow velocity and the way the probe is inserted into the aneurysm. If the size of the aneurysm is close to the size of the sample volume, the probe is likely to average together blood flowing in opposite directions, resulting in no meaningful output. Videodensitometry is even less suited to measure flow with

complex dynamics. Our conclusion is that the existing flow quantitation methods do not allow for accurate intra-aneurysmal flow velocimetry. While best attempts could be made at obtaining information on blood flow inside the aneurysm, success of such effort can not be guaranteed.

The construction of physiological models of the parent artery was performed by manually creating a piecewise–linear function which approximated flow profile obtained from intravascular Doppler strip charts. The position of the Doppler probe and its orientation were derived from anteroposterior and lateral DSA projections.

## 5.4 Models Used

In this Section the models used to validate the aneurysm blood flow simulation and the protocols used in their selection and construction will be described.

### 5.4.1 Physical System

The physical system selected for modeling was blood flow in an artery with a lateral wall aneurysm. While validation of the simulation can not be limited to the use of this type of aneurysm only, we found lateral wall aneurysms to be the most convenient for initial validation studies. The system was to be compliant with the constraints outlined in Section 3.1.

### 5.4.2 *In Vivo* Models

The *in vivo* models used for validation purposes included the common carotid artery of a swine with an attached lateral wall aneurysm surgically constructed

from a section of vein [GJM94]. These models were constructed in seven swine by members of Endovascular Therapy Service and Leo G. Rigler Research Center at the UCLA Medical Center. The selection of an artificial swine aneurysm as the *in vivo* model for validation purposes was made because of its geometric and physiologic similarity to typical human intracranial aneurysms.

Geometric and hemodynamic properties of the aneurysm-artery complex were measured using visual observation, cine-angiography and endovascular flow velocimetry. The measurements were applied towards construction of physiologic and geometric models of the artificial aneurysms.

### 5.4.3 Geometric Models

In this subsection the methods employed for geometric model construction will be covered.

#### 5.4.3.1 Data Acquisition

After construction of the aneurysm, its size and shape were visually measured and recorded. The aneurysm was imaged by acquiring DSA sequences on a *GE Advantx DLX* scanner at 30 frames per second using a 512 by 512 pixel matrix. In order to obtain better understanding of the 3–D geometry of the aneurysm, imaging was performed in lateral, anteroposterior (AP), and two 45 degree angle projections. The resulting DSA sequences were transfered over the local area network into the UCLA PACS and stored.

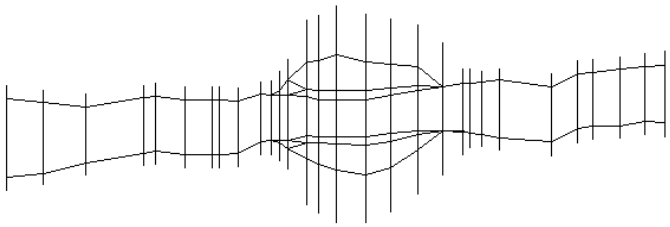

Figure 5.1: An anterioposterior projection of an aneurysm model.

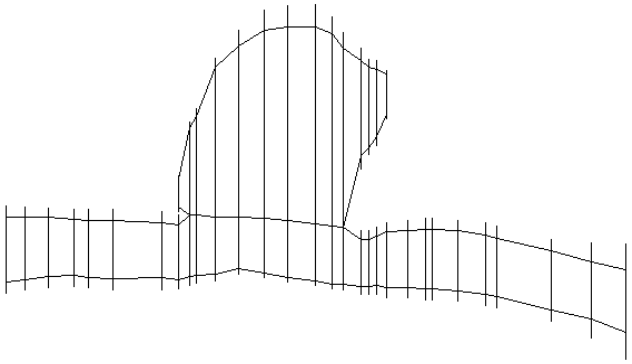

Figure 5.2: A lateral projection of an aneurysm model.

#### 5.4.3.2 Modeling

Generally, the process consisted of two parts. First, a geometric model was constructed by generating all data needed by the $NEKTON$ pre–processor $PreNEK$: the size and shape of all hexahedral spectral elements. Subsequently, $PreNEK$ was employed to build a model using the size information as the basis.

During the first step of geometric modeling, lateral and anteroposterior (AP) DSA projections of the vessel–aneurysm complex were converted into 2–D models

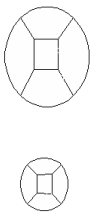

Figure 5.3: A typical slice of a hexahedral mesh. A cross–section of the vessel is in the bottom and the aneurysm is in the top.

of projections (Figures 5.1 and 5.2). The lateral projectional model was considered to be a projection of the 3–D model along its $x$ axis (across the aneurysmal neck) while the AP model was assumed to be projected along the $y$ axis (from the vessel to the aneurysm). Both projectional models consisted of rectangles perpendicular to the $z$ axis (this feature was required by $NEKTON$ software). Additional projections (beyond the AP and lateral ones) were used to resolve any inconsistencies and provide a common $z$ axis along the vessel.

The two projections were merged together along the common $z$ axis, thus generating a 3–D hexahedral mesh. Since such meshes tended not to satisfy grid quality requirements imposed by the CFD software used, the mesh was manually refined by merging or dividing neighboring slices and adjusting their elements as needed.

A typical slice of the vessel or of the aneurysm was represented by five spectral elements: four boundary ones and one in the middle (Figure 5.3 shows a slice of a typical hexahedral mesh, the aneurysm can be seen above the vessel). Special care has to be taken in order to adequately represent the aneurysmal neck (Figure

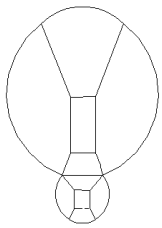

Figure 5.4: A typical slice of a hexahedral mesh. The aneurysm is atop an artery, the neck can be seen in the middle.

5.4 shows a typical mesh slice with the neck).

The constructed spectral elements were entered into $PreNEK$, the edges being curved as needed to maintain cross sectional shape. An example of the overall aneurysm geometry is shown in Figure 5.5.

Overall, the process is imprecise and time–consuming, due to the limitations of both the grid style required by the CFD software and the limitations of the imaging method used. More efficient methods were developed and tested in 1996–97 [Mar96, Mar97, Son97].

### 5.4.4 Physiologic Models

This subsection addresses to the construction of both the physiologic model of blood flow into the aneurysm (needed for simulation purposes) and the model of blood flow through the vessel–aneurysm complex (needed for validation purposes).

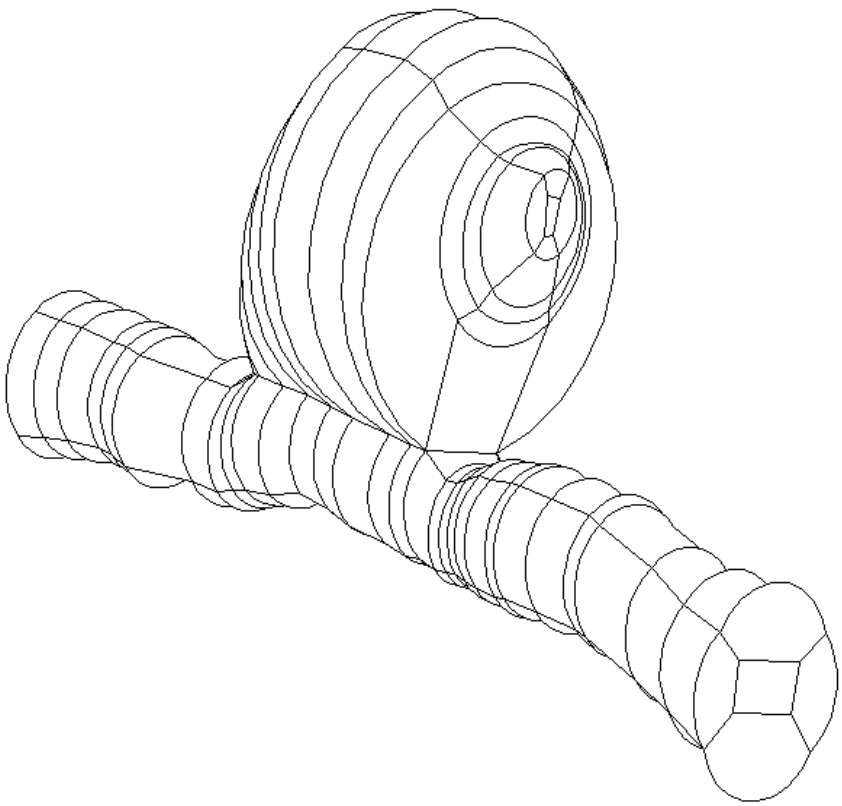

Figure 5.5: A geometric model of an aneurysm constructed in swine 895.

#### 5.4.4.1 Data Acquisition

A *Cardiometrics Flowire* intravascular ultrasonic Doppler flow meter (Section 3.3.2) was used to measure blood flow velocity at various locations inside the aneurysm and parent artery. The following locations were used:

1. Inside the vessel upstream of the aneurysm, measuring the flow into the aneurysm–parent vessel complex. This was used to generate the boundary condition on boundary segment $\Gamma_i$ (see Section 2.2.2.4).

2. Inside the vessel downstream of the aneurysm, measuring the flow out of the aneurysm–parent vessel complex.

3. Inside the vessel directly below the aneurysmal neck (Figure 5.6), measuring the part of the arterial flow bypassing the aneurysm.

4. Inside the neck near the proximal lip (Figure 5.7), measuring the flow into the aneurysm along its proximal lip.

5. In the center of the fundus inserted along the proximal lip (Figures 5.8 and 5.11), measuring flow in the fundus.

6. In the neck near the the proximal lip, facing out of the aneurysm, inserted through the neck and looped around the wall of the aneurysm (Figure 5.10). This was used to measure the flow out of the aneurysm along its proximal lip.

7. In the center of the fundus inserted through the top of the aneurysm (Figure 5.9).

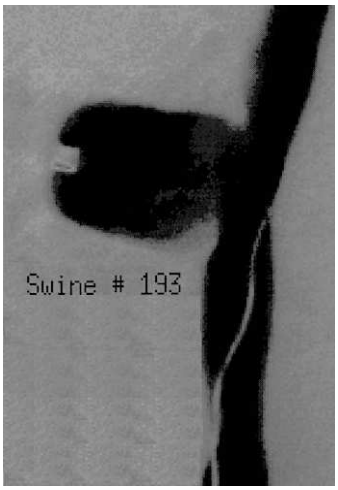


Figure 5.6: Lateral angiogram of swine 193 with probe in the vessel segment directly below the aneurysmal neck.

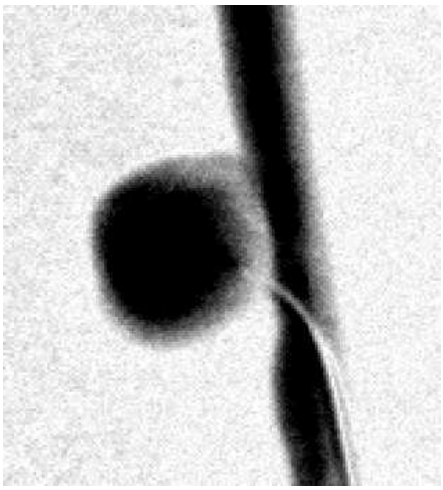

Figure 5.7: Lateral angiogram of swine 895 with probe in the neck, measuring flow into the aneurysm.

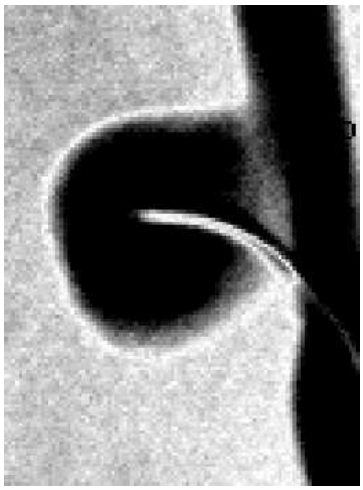

Figure 5.8: Lateral angiogram of swine 895 with probe inserted inside the aneurysm through the vessel.

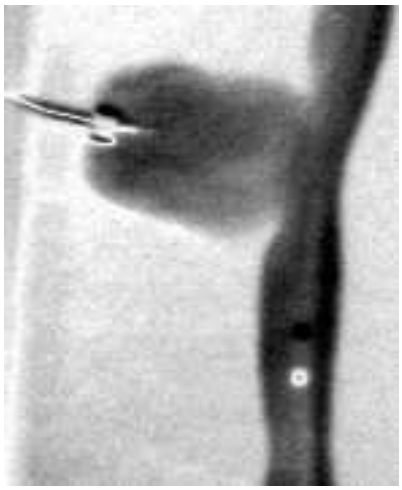

Figure 5.9: Lateral angiogram of swine 193 with probe inserted inside the aneurysm through the top of the aneurysm.

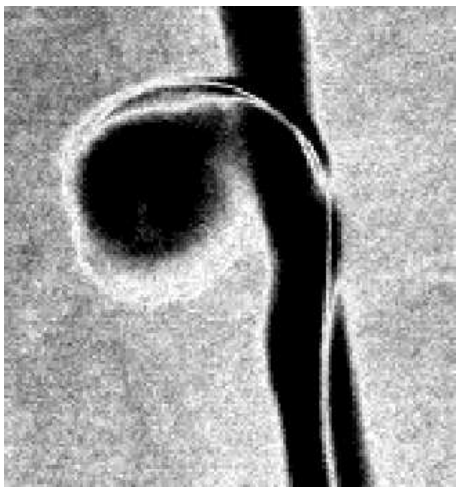

Figure 5.10: Lateral angiogram of swine 193 with probe located in the neck near its proximal lip facing out of the aneurysm (looped around the wall of the aneurysm).

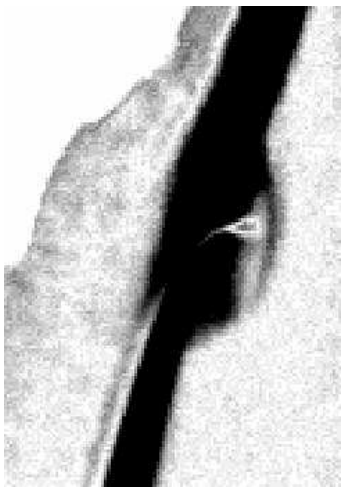

Figure 5.11: Anteroposterior angiogram of swine 895 with probe inserted inside the aneurysm through the vessel.

Mean flow velocities recorded inside the parent vessels tended to lie in the $40-60\ cm/s$ range, with peak velocities of $100-120\ cm/s$. The mean velocities recorded inside the aneurysm and its neck tended to lie within $0.5-3\ cm/s$ with peaks of $5-25\ cm/s$.

Doppler strip charts (Figure 3.5) were printed out and manually processed. The position and orientation of the probe during the measurements was measured from DSA sequences acquired during contrast injections (Figures 5.6, 5.7, 5.8, 5.9, 5.10 and 5.11).

Basic videodensitometric flow measurement (edge following) was manually employed to supplement the Doppler data.

Visual observation of DSA sequences demonstrated that at least some contrast recirculated inside the aneurysmal dome. The recirculation vortex existed even after the contrast washed out of the parental vessel.

#### 5.4.4.2 Modeling

Printed Doppler strip charts were manually approximated by piecewise–linear functions. The average number of linear segments in such functions was close to ten. For the purposes of constructing a model of blood flow into the vessel–aneurysm complex, these functions were used to generate $FORTRAN$ subroutines that computed blood flow velocity accepting time as the parameter. The subroutines were compiled into the $NEKTON$ code and used to model the boundary conditions on the inlet $\Gamma_i$.

Doppler flow velocity information was supplemented by peak arterial flow velocity information extracted from some DSA sequences by leading edge tracking.

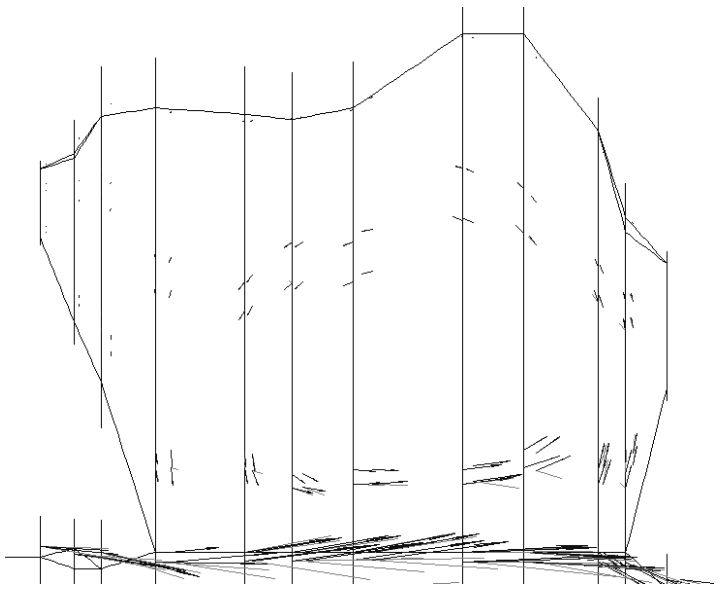

Figure 5.12: Blood recirculation inside aneurysm, swine 895.

## 5.5 Analysis of Simulation Results

The results of the simulations (Section 5.2.3 were visualized using the $PostNEK$ post–processor (Fluent Inc., Lebanon, N.H.).

### 5.5.1 Qualitative Analysis

In all 5 models examined, the flow within the aneurysm exhibited velocities by an order of magnitude lower than in the parent vessel and a complex three–dimensional structure. In most models, flow entered the aneurysm near the proximal lip, circulated inside the fundus and left near the distal lip (Figure 5.12). Stagnant blood was typically observed in the upper part of the fundus (Figure 5.13). However, is some cases a stagnant core was observed inside the recirculation vortex (Figure 5.12).

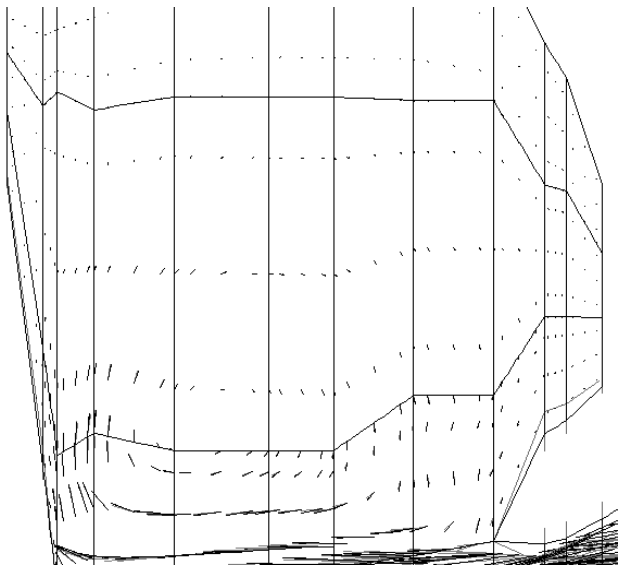

Figure 5.13: Blood recirculation inside aneurysm, swine 193. A vortex is near the distal lip, stagnant blood in the upper part of the fundus.

Secondary flows inside aneurysms (across the aneurysm) were found to achieve speeds as fast as 5-7 % of the velocity in the parent vessel. In most cases, secondary flows arose to their highest values while the flow into the parent vessel–aneurysm complex was above average, and dropped to zero after that.

Recirculation vortices were observed to change their shapes, sizes and positions with time. For example, in one model a vortex started up in the lower–distal part of the aneurysm at 0.075 *sec.* (Figure 5.14), moved to the lower–proximal part by 0.15 *sec.* (Figure 5.15), expanded to fill the whole aneurysm by 0.45 *sec.* (Figure 5.16) and almost stopped by 0.9 *sec.* (Figure 5.17). After the start of the next simulated heartbeat cycle at 1 second, the vortex reappeared in the lower–distal part, moved to the lower–proximal part by 1.125 *sec.* (Figure 5.18) and proceeded with repeating the cycle of changes. The vortex also changed from

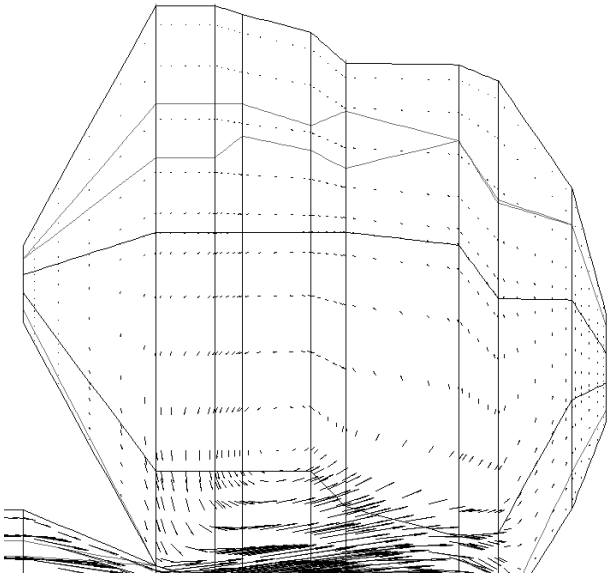

Figure 5.14: Blood recirculation inside an aneurysm, swine 687, time 0.075 $s$.

a helical to a cylindrical shape. The transition occurred after the first 20 % of the simulated heart cycle, when the blood inflow speed dropped below average.

In another model, recirculation vortices were found to appear near the proximal lip (Figure 5.19) and to dominate the flow inside the aneurysm after the inflow velocity dropped below its average level (0.20 $sec.$ and later).

The variation of pressure within the simulated object was found to be low, with a gradual pressure decrease from the intake to the outlet. Since the high inlet pressure can be explained by the plug flow in the inlet, and the subsequent pressure drop can be explained by the transition of flow from plug to parabolic, such pressure map is normal.

The solution divergence was found to be virtually constant through the computational domain, with increases along the boundaries of spectral elements in

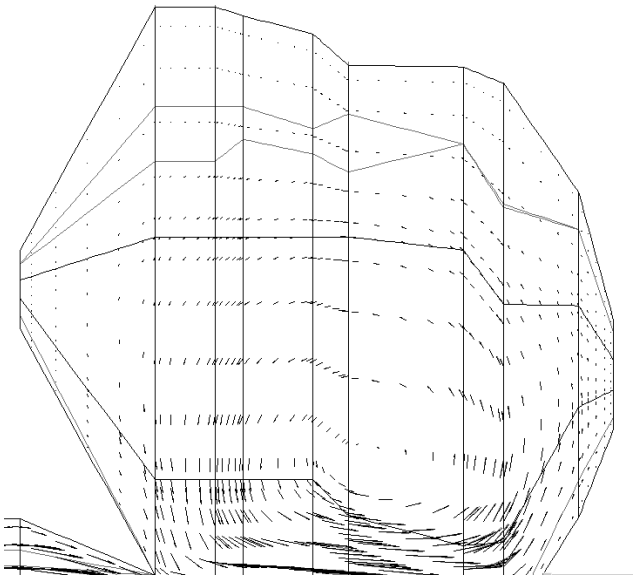

Figure 5.15: Blood recirculation inside an aneurysm, swine 687, time 0.15 $s$.

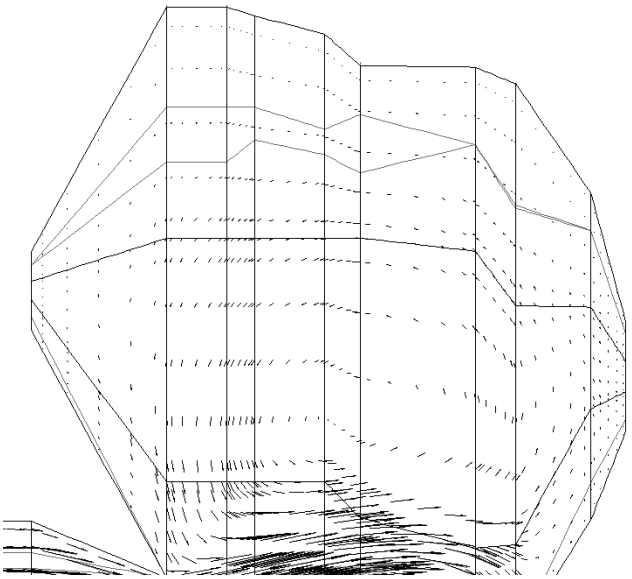

Figure 5.16: Blood recirculation inside an aneurysm, swine 687, time 0.45 $s$.

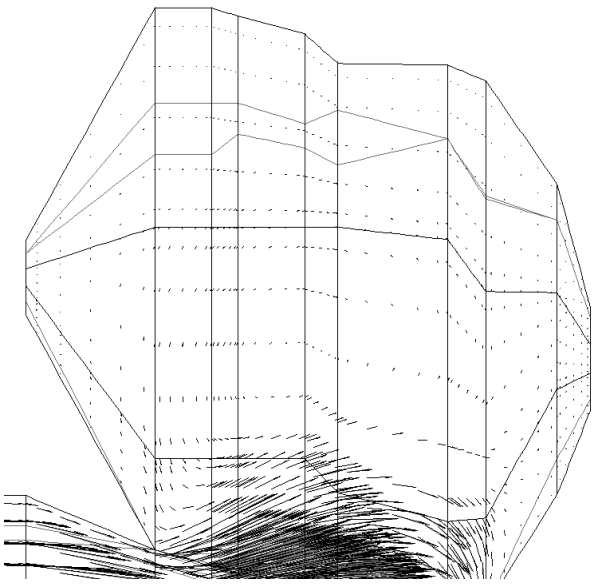

Figure 5.17: Blood recirculation inside an aneurysm, swine 687, time 0.9 $s$.

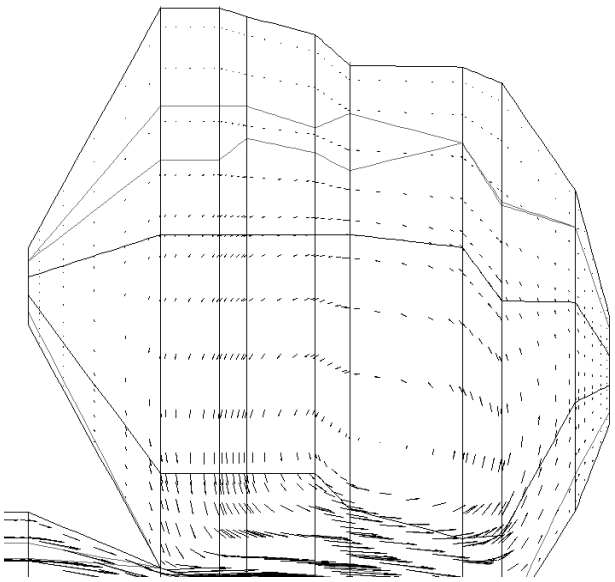

Figure 5.18: Blood recirculation inside an aneurysm, swine 687, time 1.125 $s$.

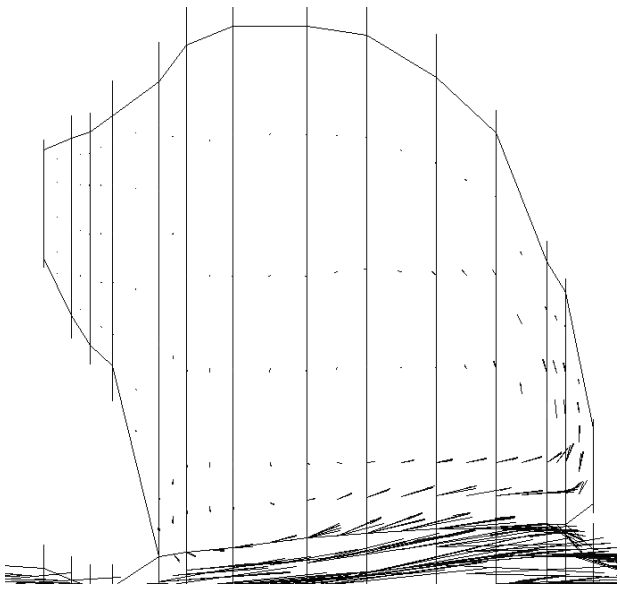

Figure 5.19: Blood recirculation inside aneurysm, swine 66, time 1.05 $s$.

areas with high solution gradients (mostly in the neck and near the inlet). Minor solution wiggles were occasionally observed in the higher–divergence areas. The reduction in solution quality along such spectral element boundaries appears to be inherent to the spectral element method. It may be explained by the fact that the regionally defined basis function become less efficient near the boundary of their region of definition. While this problem might be resolved by increasing mesh density in affected areas, the meshing limitations of $NEKTON$ software in most cases made such an increase prohibitively expensive in terms of both manual labor and computational expenses.

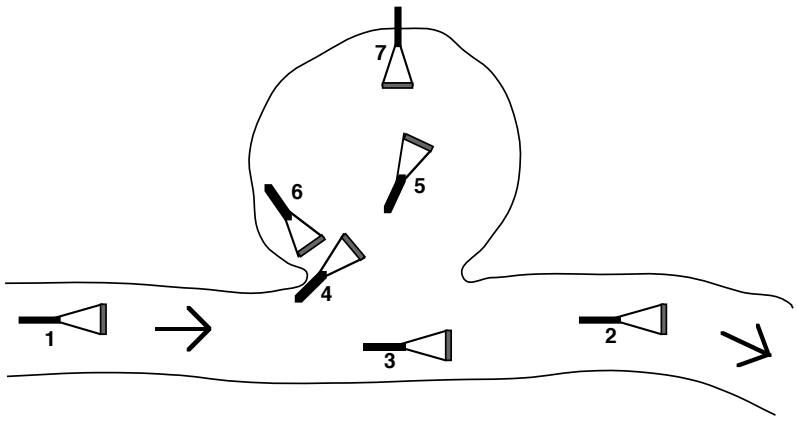


Figure 5.20: Different Doppler probe positions inside the aneurysm and the parent vessel (sampling volumes not to scale).

### 5.5.2 Quantitative Analysis

As described in Section 5.4.4.1, quantitative flow measurements (employing an intravascular ultrasonic Doppler flow meter) were performed for each model at seven distinct areas within the aneurysm and the parent vessel (shown in Figure 5.20). Bi–planar DSA angiograms were used to determine the location of the probe. The total number of measurements per model varied due to unavailability of access through the top of the aneurysm for early models and due to multiple measurements performed in the same areas. In some angiographic sequences traveling contrast occluded the probe, making it impossible to determine its position and direction.

Flow speeds near the axis of the parent vessel tended to be close to speeds at the inlet of the parent vessel (provided to the simulation as a boundary condition).

As for the flow inside the aneurysm, numerical comparison demonstrated a wide variety of results, ranging from a complete failure to predict the character

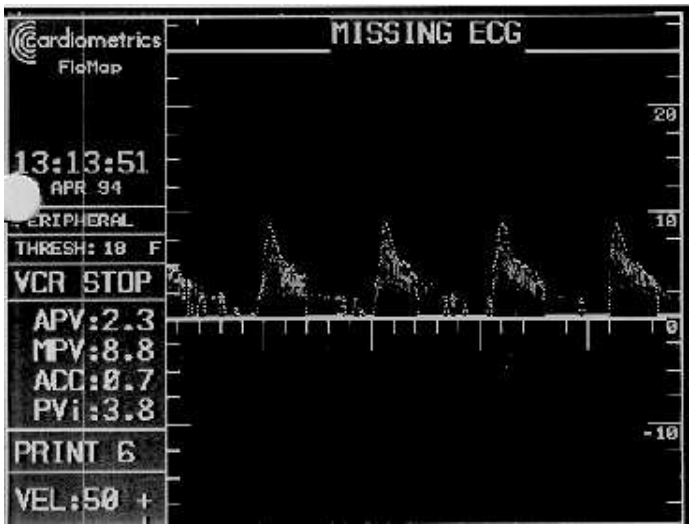


Figure 5.21: Doppler strip chart of swine 895 with probe in position 7.

of flow (Doppler flow chart and comparison of the numerical and Doppler data shown in Figures 5.21 and 5.22 respectively) to a crude approximation of the experimental flow chart (Figures 5.23 and 5.24).

In some cases, the numerical speeds were lower than the experimental ones by three orders of magnitude, while in a few cases the numerical flow appeared as a dampened version of the experimental, having constant area below the speed curve (Figures 5.25 and 5.26).

In almost all cases the probe was found to be resting against a wall, the location of which was modeled crudely, especially in the middle of faces of spectral elements. Both the position and the direction of the probe were also imprecise. The distance between the numerical flow measurement point and the computational domain boundary was probably lower than the distance between the tip of the probe and the wall. If that was the case, numerical speed near the measurement points would have been slowed down because of wall proximity. It was

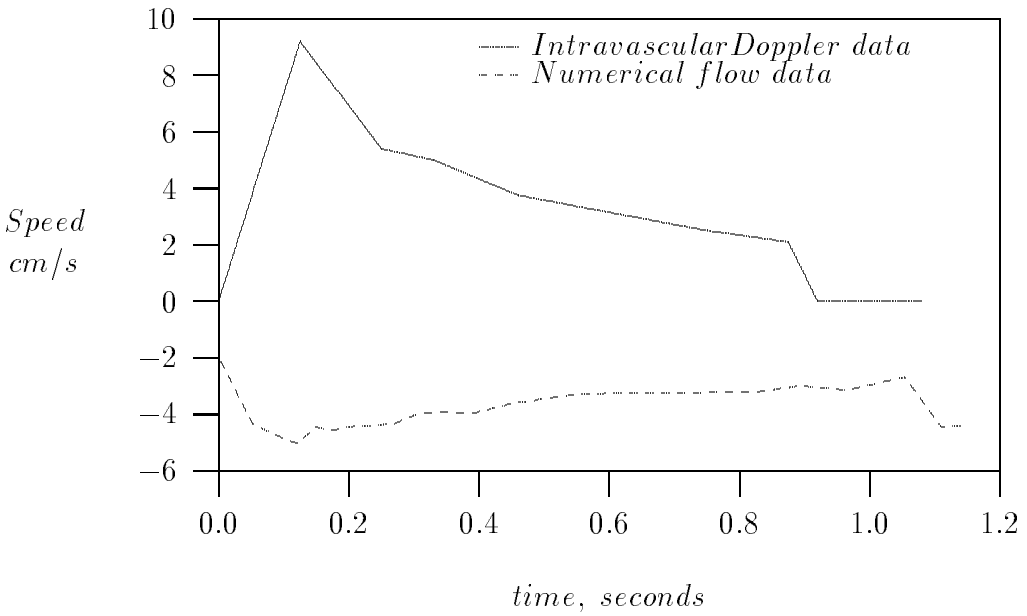


Figure 5.22: Numerical and experimental blood flow speed in swine 895 with Doppler probe in position 7.

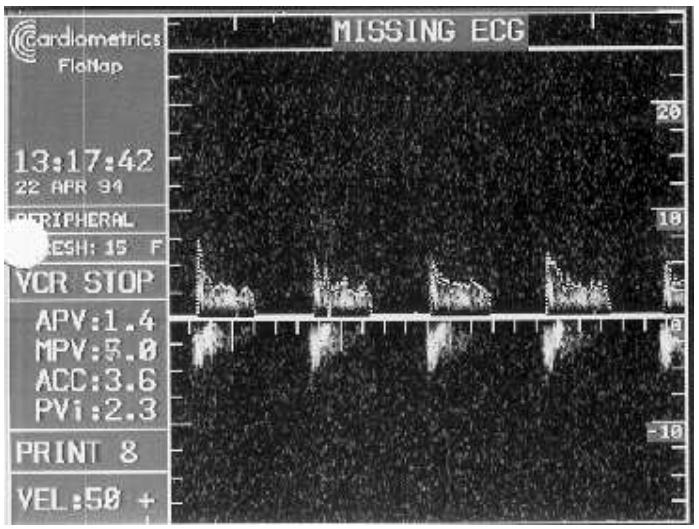


Figure 5.23: Doppler strip chart of swine 895 with probe in position 4.

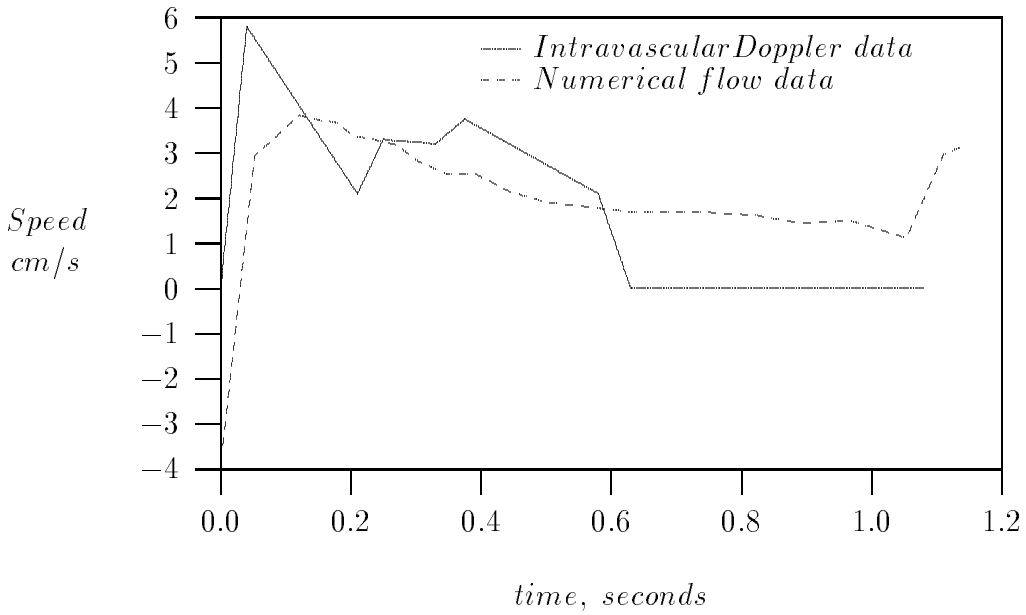


Figure 5.24: Numerical and experimental blood flow speed in swine 895 with Doppler probe in position 4.

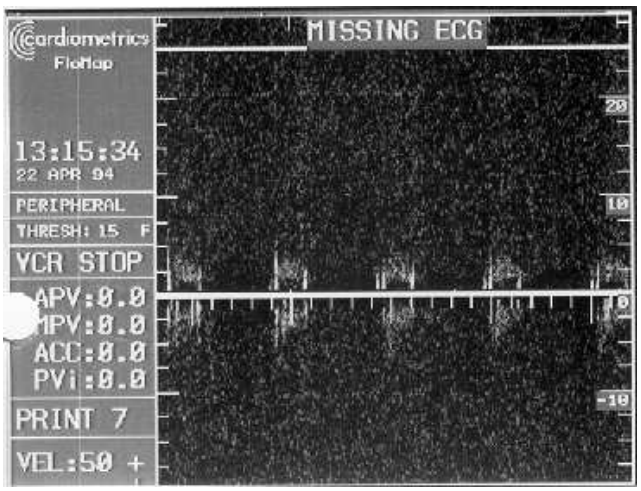


Figure 5.25: Doppler strip chart of swine 895 with probe in position 5.

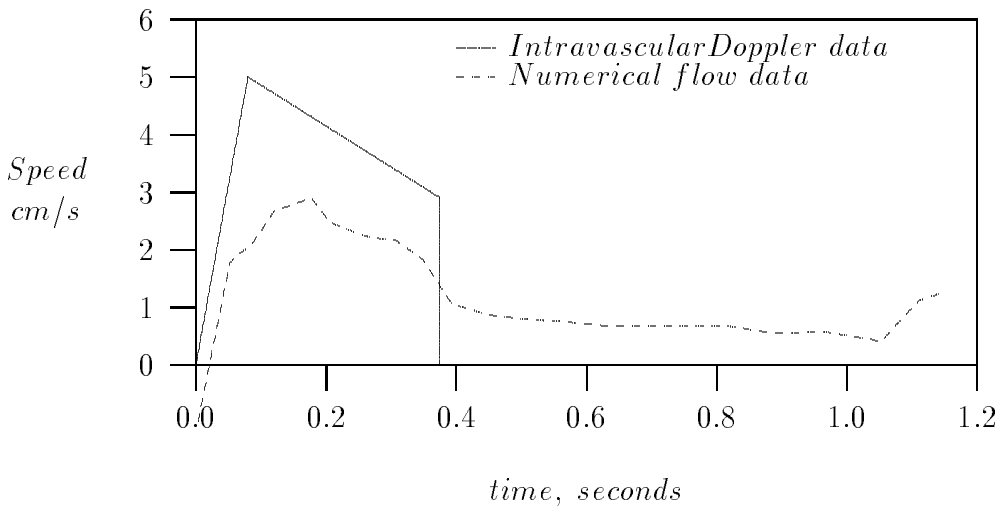


Figure 5.26: Numerical and experimental blood flow speed in swine 895 with Doppler probe in position 5.

speculated that such probe mispositioning was the primary reason for the major differences between numerical and experimental flows.

For some flow measurements performed on model 895, errors were approximately calculated for position and direction of the Doppler probe and for the position of the wall. Instead of recording numerical flow in one point, it was recorded at numerous locations throughout the region where the tip of the Doppler probe may have been located. The resulting measurements demonstrated that numerical flow differed significantly between neighboring locations. Figure 5.28 shows the differences between flows in three possible probe locations and the Doppler flow data from the chart shown in Figure 5.27. In most cases, selection of the measurement point within the area of uncertainty allowed numerical flow to approach the shape and magnitude of the expeimental flow profile (Figures 5.29 and 5.30).

Any validation dependent on arbitrary choice of sample location can not be

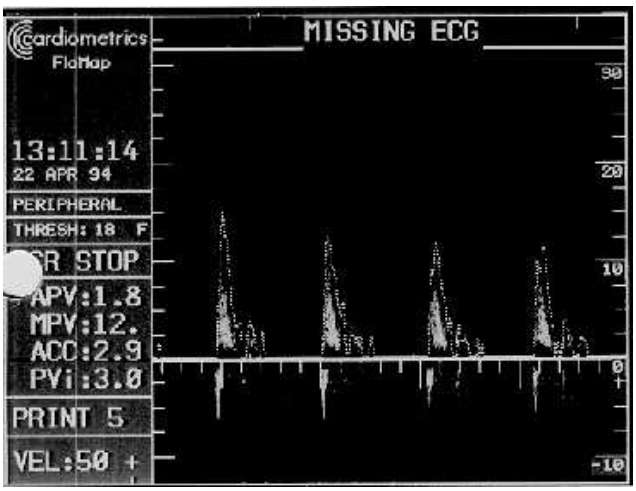


Figure 5.27: Doppler strip chart of swine 895 with probe in position 4.

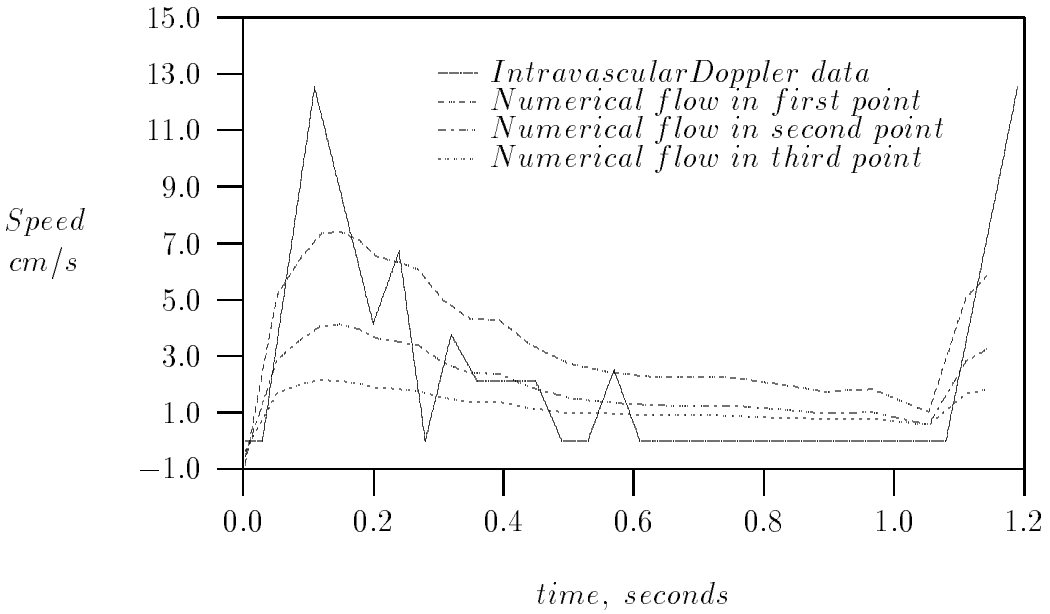


Figure 5.28: Blood flow speed in swine 895. The Doppler probe is in position 4, the numerical flow was measured in three points close to the tip of the probe.

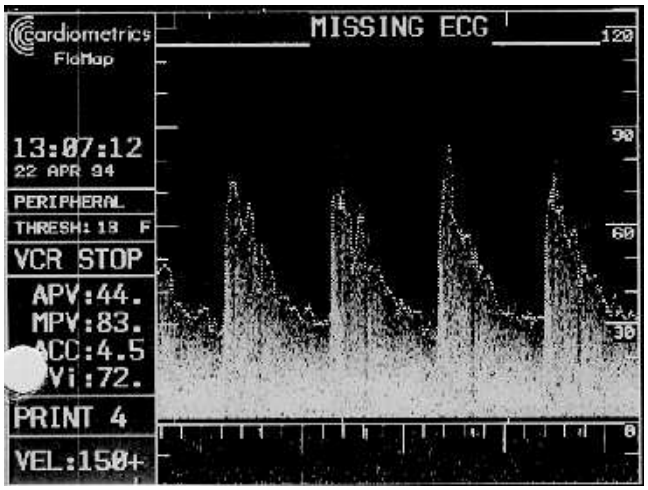


Figure 5.29: Doppler strip chart of swine 895 with probe in position 2.

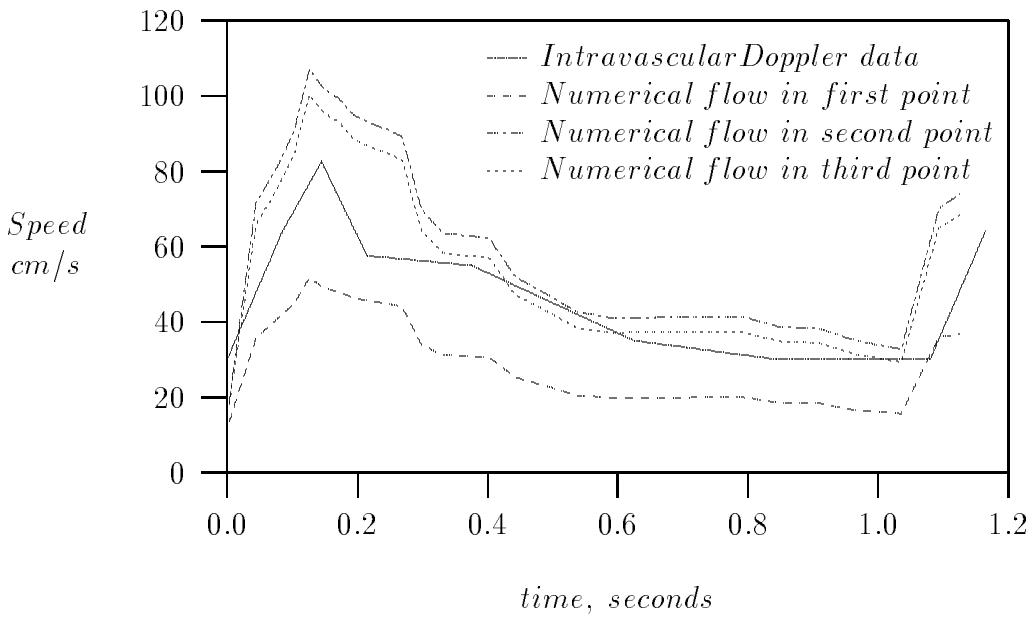


Figure 5.30: Blood flow speed in swine 895. The Doppler probe is in position 2, the numerical flow was measured in three points close to the tip of the probe.

considered conclusive, especially if the simulation samples were selected to be closest to the experimental ones. While it is not impossible that the best–fit location does correspond to the original location of the probe, there is no way to prove or disprove this. It was considered that quantitative validation is impossible without a valid way of selecting the point in which numerical flow is measured for the purposes of comparing it with Doppler flow speed data. Since the Doppler probe averages flow speeds inside a sampling volume with a size comparable to that of an aneurysm (Section 3.3.2), it was proposed to develop a software tool that would simulate the functionality of a Doppler probe. Such a "virtual Doppler probe" could be positioned inside the aneurysm and would average the numerical flow component parallel to its axis throughout its sampling volume. While both the true location and true direction of the probe would still be unknown within the area of uncertainty, the size of the sampling volume of the virtual probe should reduce the number of possible locations and directions to be considered.

While a virtual Doppler probe is likely to underestimate flow since it would average flow speed values in collocation points and may miss greater flow speeds between such points, it would still be more effective validation tool than one–point numerical flow measurements. Virtual Doppler probe was implemented by Harreld as part of a virtual reality visualization engine and used in further validation studies [Har96].

Another problem resulting from possible uncertainty in position and direction of the Doppler probe is that the flow into the inlet of the parent vessel may be underestimated if the tip of the probe is resting against the wall. The only solution proposed for this problem involved calculating a number of different inflow speeds and performing simulation with different inlet boundary conditions.

Comparison of simulation results demonstrated that for most models, flow speeds near the axis of the parent vessel changed linearly with respect to changes in the inlet speeds while speeds inside the aneurysms sometimes changed nonlinearly.

As it was already demonstrated, any quantitative comparison of numerical and experimental flow speeds encounters double uncertainty: one the one hand, both the location and orientation of the Doppler probe are uncertain, and on the other hand, numerical flow in any point is also uncertain due to uncertainty in the inflow speeds. This double uncertainty makes conclusive quantitative validation impossible. If quantitative validation is desired, certain steps must be taken to reduce uncertainty. Such steps may include improving precision of geometric modeling, developing ways of determining the location and direction of the Doppler probe with greater accuracy, and using physiologic modeling procedures with greater spatial accuracy (based on, for example, videodensitometry).

# CHAPTER 6

# Conclusion

## 6.1 Overview

The purpose of this thesis was to study and evaluate computational techniques used to perform brain aneurysm blood flow simulations and ensure their validity.

Several surgically constructed *in vivo* aneurysm models were used to simulate pulsatile flow of Newtonian blood through them. Geometric modeling of three–dimensional rigid aneurysms was performed using bi–planar X–ray digital angiography and visual measurements. Structured hexahedral volume meshes were built manually. Physiologic modeling was performed using intravascular Doppler ultrasonic flow velocimetry in several locations per model. The measurement point locations were also determined using bi–planar X–ray digital angiography. Alternative modeling procedures were discussed and evaluated.

Aneurysm blood flow was simulated using a commercial computational fluid dynamics software package. A laminar formulation of the Navier-Stokes equation was applied to model the three–dimensional transient flow. Blood flow patterns observed included distal inflow, proximal outflow, helical and cylindrical rotation, and stagnant core areas inside the aneurysm. Numerical flow was compared to the flow speed observations generated by a Doppler flow meter.

## 6.2 Discussion

The goals of this thesis (Section 1.3) included a study and validation of various computational techniques used in preparing and performing brain aneurysm blood flow simulations.

The blood flow patterns observed inside the simulated aneurysms were found to match *in vivo* results (cineangiography and intravascular Doppler flow velocimetry of the swine aneurysms). The were also found to match the patterns reported in *in vivo* ([SGR92], [MSO92]), *in vitro* ([NKS84], [LSP87], [SPL87]) and numerical ([Ort96], [PPR89], [LPR93],[KN96],[GCO92],[TY94] and [Har93]) studies. The flow was found to recirculate inside the aneurysmal dome, leaving a sizeable volume of stagnant blood. The recirculation speeds were lower than the speeds of arterial flow by at least one order of magnitude. The recirculation vortices were observed to change positions, sizes and shapes with time. Flow patterns observed in aneurysms of different shapes were different. Secondary flows inside the aneurysms were observed to change with time and achieve significant speeds at some times. The most likely, they were caused by the asymmetric shapes of the modeled aneurysms. Changes in inflow speeds caused the shapes and speeds of aneurysmal flow to change non-linearly.

Quantitatively, numerical flow speeds did not match the experimental data. Observed errors achieved values in excess of 200 %. While for some measurement points average numerical flow was found to lie within 10% of the average experimental flow, the uncertainty in the position and direction of the Doppler probe and in the inflow speed made such numerical comparisons inconclusive. It was concluded that until better quantitative validation tools are developed, validation must be restricted to independent validation of all individual techniques involved

in the simulation process and to qualitative validation of the overall process.

The physiologic modeling procedure used in this thesis was found to be grossly inadequate for quantitative validation proposes. While intravascular Doppler flow velocimetry is known to be accurate and reliable, both the position and direction of the Doppler probe could not be determined without significant uncertainty. Since quantitative validation involves a comparison of experimental flow with numerical flow that is measured in an uncertain location, projected at an uncertain angle and was simulated using uncertain inflow speed, the numerical flow has too high uncertainty for conclusive quantitative validation. Better physiologic modeling tools and protocols should be able to reduce the numerical uncertainty.

The geometric modeling procedure used in this thesis involved manual geometry reconstruction from bi–planar DSA sequences. It was found to produce inadequate information about the geometry of the aneurysm, especially in the neck, due to the loss of 3–D information in projections. It was also found to be grossly inadequate in determining both the location and orientation of the tip of the intravascular Doppler probe, adding significant geometric uncertainty into physiologic models constructed using bi–planar DSA. A more precise geometric modeling would be based on an inherently 3–D imaging modality such as CT or MR. While DSA is the only medical imaging modality available to interventional neurologists during a surgery, and it is likely to remain so until at least the beginning of the 21-st century, all ways of increasing the amount of geometric information in DSA sequences should be explored. They may include the study of acquisition protocols allowing for better observability of the Doppler tip and the use of truly bi–planar DSA (where the two projections are acquired in an interleaved manner by using two X-ray source–detector pairs simultaneously) as

opposed to repositioning the camera and the table with the trial animal between sequences. Eventually, DSA usefulness for geometric modeling should be limited to the determination of the spatial orientation of the aneurysm.

Regular hexahedral spatial meshes were also found to be inadequate for brain aneurysm blood flow modeling. The restrictions imposed by mesh regularity were found to result in meshes with insufficient density in high–gradient zones and excessive density in low–gradient zones. The former problem resulted in the loss of information and solution accuracy, causing the CFD software to reduce the temporal step thus increasing the computational time, while the latter problem caused excessive computations to be performed. The typical time necessary to simulate brain aneurysm blood flow for 1.5 heart cycles on a *SPARCstation-10* (Sun Microsystems, Mountain View, CA) varied between 5 and 7 days, which is unacceptable for clinical use. The process of mesh refinement was found to be cumbersome and time–consuming. An unstructured tetrahedral mesh would allow for easy modification (including mesh adaptation during a simulation) and improved solution accuracy without requiring excessive computational time.

Transient 3–D Navier-Stokes equations in laminar formulation were found to be adequate for brain aneurysm blood flow modeling. Any simplification of that model is likely to result in the loss of crucial information (for example, the use of a 2–D model would result in the loss of all information regarding secondary flows). It was determined that a commercial general purpose computational fluid dynamics (CFD) software package can be used to simulate brain aneurysm blood flow.

Thresholding was found to provide adequate segmentation for *in vivo* DSA images as well as CT and MR images of aneurysm phantoms. However, prelim-

inary studies demonstrated the inadequacy of thresholding for segmentation of CT and MR images of *in vivo* aneurysms.

## 6.3 Contributions

The following contributions were made while performing this study:

- Pulsatile laminar flow of Newtonian blood through rigid lateral wall intracranial aneurysms was simulated using computational fluid dynamics.
- Procedures and computational techniques for geometric and physiologic modeling of brain aneurysms were evaluated.
- Qualitative and quantitative validation was performed using exprerimental measurements as well as the results of previous studies.
- New validation tools were proposed.

## 6.4 Suggestions for Further Research

The next steps in this research need to concern improvements in model realism and accuracy, both by using more realistic mathematical models, by improving precision of modeling procedures and by simulating the models in a more accurate way.

Realism of the mathematical model may be increased by taking into account the non–Newtonian properties of blood and the elastic properties of aneurysmal and vascular walls. Simulations performed by Low et al. [LPR93], Perktold et al. [PPR89] and Chitanvis et al. [CHP95] demonstrated that accounting for these properties can alter the simulated flow significantly.

The accuracy of the simulation can be improved by using adaptive irregular meshes. Such meshes can also be more accurate and realistic than the unstructured ones due to the elimination of many cumbersome constraints imposed on the latter.

A set of models can not be considered realistic if it consists of aneurysms belonging to only one type, especially a type observed in less than one quarter of described cases. The validation effort should include at least some of the more frequent intracranial aneurysm types, such as bifurcation and terminal.

The accuracy of the methods used to acquire both the geometric and physiologic information also needs to be improved. The former should be capable of determining the position and direction of the Doppler probe as well as the position and shape of endovascular coils so that their insertion into aneurysms can also be simulated. The latter should be capable of producing instantaneous measurements of blood flow through both the parent vessel and the aneurysm in relatively small sampling volumes.

# References


[AET93] C.M. Anderson, R.R. Edelman, and P.A. Turski. *Clinical Magnetic Resonance Angiography*. Raven Press, New York, 1993.

[AS95] G. Austin and W. Schievink. "Biomathematical simulation of brain aneurysm blood flow." *FASEB Journal*, **9**:A13, 1995.

[BM90] P.K. Banerjee and L. Morino, editors. *Boundary Element Methods in Nonlinear Fluid Dynamics*. Elsevier Applied Sciences, New York, NY, 1990.

[BP83] B.R. Baliga and S.V. Patankar. "A Control-Volume Finite-Element Method for Two-Dimensional Fluid Flow and Heat Transfer." *Numerical Heat Transfer*, **6**:245–61, 1983.

[BP95] C.A. Burbeck and S.M. Pizer. "Object representation by cores: identifying and representing primitive spatial regions." *Vision Res*, **35**:1917–30, 1995.

[Bro84] W.R. Brody. *Digital Radiography*. Raven Press, New York, 1984.

[Bus83] G.Y. Buss. "Transition to turbulence." In D.E.M. Taylor and A.L. Stevens, editors, *Blood Flow:Theory and Practice*, chapter 2, pp. 7–38. Academic Press, London, 1983.

[CDV92] Robert A. Close, Gary R. Duckwiler, and Fernando Viñuela. "Fluid equations applied to blood flow measurement using digital videodensitometry." *Investigative Radiology*, **27**:504–9, 1992.

[Cha82] J.H. Chamberlain. "Cardiac output measurement by indicator dilution." In R.T. Mathie, editor, *Blood Flow Measurement in Man*, chapter 4, pp. 37–49. Castle House, London, 1982.

[CHB86] A.C. Colchester, D.J. Hawkes, J.N.H Brunt, G.H. du Boulay, and A. Wallis. "Pulsatile flow measurements with the aid of 3–D reconstructions from dynamic angiographic recordings." In S.L. Bacharach, editor, *Information Processing in Medical Imaging*, volume 9, pp. 247–65, 1986.

[CHP95] S.M. Chitanvis, G. Hademenos, and W.J. Power. "Hemodynamic assessment of the development and rupture of intracranial aneurysms

using computational simulations." *Neurological Research*, **17**:426–34, 1995.

[CHQ88] C. Canuto, M.Y. Hussaini, A. Quarteroni, and T. Zang. *Spectral Methods in Fluid Dynamics*. Springer Series in Computational Physics. Springer–Verlag, New York, NY, 1988.

[Cli97] H. Cline. "Recent Advances in Segmentation." Talk at the March 1997 GE Research Workstation Meeting. Currently available at *http://www.crd.ge.com/rws/meetings/talks/LaJollaMar97/ Cline-Mar97/segment.html*, 1997.

[CPS78] C.G. Caro, T.J. Pedley, R.C. Schroter, and W.A. Seed. *The Mechanics of the Circulation*. Oxford University Press, Oxford, 1978.

[Cri94] John Cristy. "ImageMagick." Currently available at *http://ftp.x.org: contrib/applications/ImageMagick/ImageMagick-3.0.tar.gz*, 1994.

[CVK94] J.C. Chaloupka, F. Viñuela, C. Kimme-Smith, J. Robert, and G. Duckwiler. "Use of a Doppler guide wire for intravascular blood flow measurements: a validation study for potential neurologic endovascular applications." *American Journal of Neuroradiology*, **15**:509–17, 1994.

[dBC86] G.H. du Boulay, J. Brunt, A. Colchester, D. Hawkes, A. Wallis, and D. Wicks. "Volume flow measurement of pulsatile flow by digitized cine angiography." *Acta Radiologica*, **369**:59–62, 1986.

[DCP92] J.W. Doucette, P.D. Corl, H.M. Payne, A.E. Flynn, M. Goto, M. Nassi, and J. Segal. "Validation of a Doppler guide wire for intravascular measurement of coronary artery blood flow." *Circulation*, **85**:1899–911, 1992.

[Din85] L. Dintenfass. *Blood Viscosity, Hyperviscosity and Hyperviscosaemia*. MTP Press Limited, Lancaster, 1985.

[DW94] J.F. Dannehoffer and N.P. Weatherill. "Techniques for visual evaluation of computational grids." In N.P. Weatherhill, editor, *Grid Generation. Lecture series 1994-02*, chapter 5, pp. 1–19. von Karman Institute for Fluid Dynamics, Rhode Saint Genese, 1994.

[Ebe96] D. Eberly. *MAGIC: An Object-Oriented Library for Image Analysis*. User's Manual, University of North Carolina, Chapel Hill. Computer Science Department, 1996.

[EGM94] D. Eberly, R.B. Gardner, B.S. Morse, S.M. Pizer, and C. Scharlach. "Ridges for image analysis." *Journal of Mathematical Imaging And Vision*, **4**:351–71, 1994.

[FHS79] U. Fermor, H. Huber, F.K. Schmiel, and P. Spiller. "Measurement of flow velocity n the model circulation by videodensitometry." *Basic Res Cardiol*, **73**:361–77, 1979.

[Flu92] Fluent Inc., Lebanon N.H. *NEKTON 2.85 User's Guide*, 1992.

[Flu94a] Fluent Inc., Lebanon N.H. *FLUENT/UNS 1.0 User's Guide*, 1994.

[Flu94b] Fluent Inc., Lebanon N.H. *TGrid 2.2 User's Guide*, 1994.

[Flu95] Fluent Inc., Lebanon N.H. *FLUENT 4.3 User's Guide*, 1995.

[Flu96] Fluent Inc., Lebanon N.H. *User's Guide for FLUENT/UNS and Rampant, Release 4.0*, 1996.

[Fox83] J.L. Fox. *Intracranial Aneurysms*, volume 1. Springer-Verlag, New York, 1983.

[FR72] G.G. Ferguson and M.R. Roach. "Flow Conditions at Bifurcations as Determined in Glass Models, with Reference to the Focal Distributions of Vascular Lesions." In D.H. Bergel, editor, *Cardiovascular Fluid Dynamics*, volume 2, chapter 14, pp. 141–56. Academic Press, London, Great Britain, 1972.

[Fre95] C.J. Freitas. "Perspective: Selected benchmarks from commercial CFD codes." *Transactions of the ASME*, **117**:208–18, 1995.

[Fro85] C.-E. Froberg. *Numerical Mathematics*. Benjamin/Cummings, Menlo Park, 1985.

[GCO92] C.F. Gonzalez, Y.I. Cho, H.V. Ortega, and J. Moret. "Intracranial aneurysms: Flow analysis of their origin and progression." *American Journal of Neuroradiology*, **13**:181–8, 1992.

[GE 96] GE Medical Systems, Waukesha, WI. *GE Research Workstation User's Manual*, 1996.

[GJM94] G. Guglielmi, C. Ji, T.F. Massoud, A. Kurata, S.P. Lownie, F. Viñuela, and J. Robert. "Experimental saccular aneurysms. II. A new model in swine." *Neuroradiology*, **36**:547–50, 1994.

[GVD91] G. Guglielmi, F. Viñuela, J. Dion, and G. Duckwiler. "Electrothrombosis of saccular aneurysms via endovascular approach. Part 2: Preliminary clinical experience." *Journal of Neurosurgery*, **75**:8–14, 1991.

[GVD92] G. Guglielmi, F. Viñuela, G. Duckwiler, J. Dion, P. Lylyk, A. Berenstein, C. Strother, V. Graves, V. Halbach, and D. Nichols. "Endovascular treatment of posterior circulation aneurysms by electrothrombosis using electrically detachable coils." *Journal of Neurosurgery*, **77**:515–24, 1992.

[GVS91] G. Guglielmi, F. Viñuela, I. Sepetka, and V. Macellari. "Electrothrombosis of saccular aneurysms via endovascular approach. Part 1: Electrochemical basis, technique and experimental results." *Journal of Neurosurgery*, **75**:1–7, 1991.

[Har93] Michael R. Harreld. *"Computer Simulation of Blood Flow in an Intracranial Aneurysm."*. Master's thesis, University of California, Los Angeles, Computer Science Department, 1993.

[Har96] Michael R. Harreld. *Brain Aneurysm Blood Flow: Modeling, Simulation, VR Visualization*. PhD thesis, University of California, Los Angeles, Computer Science Department, 1996.

[HD90] K.R. Hoffman and K. Doi. "A new angiographic technique for measurement of instantaneous blood flow rates using distance-density curves." *SPIE 1990*, **1233**:240–3, 1990.

[HS94] R.M. Haralick and L.G. Shapiro. "Glossary of computer vision terms." In E.R. Dougherty, editor, *Digital Image Processing Methods*, chapter 11, pp. 415–467. Marcel Dekker,Inc., New York, 1994.

[HSC94] D.J. Hawkes, A.M. Seifalian, A.C. Colchester, N. Iqbal, C.R. Hardingham, C.F. Bladin, and K.E.F. Hobbs. "Validation of volume blood flow measurements using three- dimensional distance-concentration functions derived from digital x-ray angiograms." *Investigative Radiology*, **29**:434–42, 1994.

[HT92] H.K. Huang and R.K. Taira. "Infrastructure design of a picture archiving and communication system." *American Journal of Roentgenology*, **158**:743–9, 1992.

[HTL93] H.K. Huang, R.K. Taira, S.L. Lou, A.W. Wong, C. Breant, K.S. Chuang, B.K. Stewart, K. Andriole, and R. Tecotzky. "Implementation of a large-scale picture archiving and communication system." *Computerized Medical Imaging and Graphics*, **17**:1–11, 1993.

[Jah93] Bernd Jahne. *Digital Image Processing. Concepts, Algorithms and Scientific Applications.* Springer-Verlag, Berlin-Heidelberg-New York, 1993.

[KN95] B.V.R. Kumar and K.B. Naidu. "Finite Element Analysis of Nonlinear Pulsatile Suspension Flow Dynamics in Blood Vessels with Aneurysm." *Computers in Biology and Medicine*, **25**:1–20, 1995.

[KN96] B.V.R. Kumar and K.B. Naidu. "Hemodynamics in Aneurysm." *Computers and Biomedical Research*, **29**:119–39, 1996.

[Kri95] Serge D.C. van Kriekinge. *"Image Processing for Blood Flow Quantification."*. Master's thesis, University of California, Los Angeles, Computer Science Department, 1995.

[KS79] L Kreel and R.E. Steiner. *Medical Imaging.* Yearbook Medical Publishers Inc., Aylesbury, 1979.

[LH92] S.L. Lou and H.K. Huang. "Assessment of a neuroradiology picture archiving and communication system in clinical practice." *American Journal of Roentgenology*, **159**:1321–7, 1992.

[Liu97] Damon Liu. "Scientific Visualization of Large Time-Dependent Flow Datasets in Medical Virtual Reality Systems." Currently available at *http://www.radsci.ucla.edu: 8000/aneurysm/damon.html*, 1997.

[LPR93] M. Low, K. Perktold, and R. Raunig. "Hemodynamics in rigid and distensible saccular aneurysms: a numerical study of pulsatile flow characteristics." *Biorheology*, **30**:287–98, 1993.

[LSP87] D.W. Liepsch, H.J. Steiger, A. Poll, and H.J. Reulen. "Hemodynamic stress in lateral saccular aneurysms." *Biorheology*, **24**:689–710, 1987.

[LTS92] K.L. Lanzieri, R.W. Tarr, W.R. Selman, A.S. Smith, and M.H. Naheedy. "Use of the Delayed MAsk for Improved Demonstration of Aneurysms on Intraarterial DSA." *American Journal of Neuroradiology*, **13**:1589–1593, 1992.

[Mar96] Branko Marovic. "The Report on Work at UCLA and a Description of Developed Programs." Currently available at *http://www.radsci.ucla.edu: 8000/aneurysm/branko.html*, 1996.

[Mar97] Branko Marovic. Personal communication, 1997.

[Mat93] T. Matsuzawa. "Finite element analysis in three-dimensional flow through a lateral saccular aneurysm." *Frontiers of Medical and Biological Engineering*, **5**:89–94, 1993.

[Max82] K.J. Maxted. "Electromagnetic flowmetry." In R.T. Mathie, editor, *Blood Flow Measurement in Man*, chapter 7, pp. 71–79. Castle House, London, 1982.

[MD95] Tom Malisch and Gary Duckwiler. *What you should know about aneurysms*. Division of Endovascular Therapy, University of California, Los Angeles, 1995.

[MPL93] B.S. Morse, S.M. Pizer, and A. Liu. "Multiscale Medial Analysis of medical images." In H.H. Barrett and A.F. Gmitro, editors, *Information Processing in Medical Imaging*, pp. 112–31, 1993.

[MSO92] H. Matsuoka, Y. Shigematsu, T. Ohtani, T. Sumimoto, M. Hamada, K. Hiwada, H. Miki, and K. Sadamoto. "Analysis of blood flow patterns in aortic aneurysm by cine magnetic resonance imaging: A review of case material." *Angiology*, **43**:181–7, 1992.

[NKS84] H. Niimi, Y. Kawano, and I. Sugiyama. "Structure of blood flow through a curved vessel with an aneurysm." *Biorheology*, **21**:603–15, 1984.

[NR95] T. Naidich and A. Righi. "Neurovascular Imaging." In B. Katzen, G. Becker, J. Benenati, and G. Zemer, editors, *Vascular Imaging.*, number 33:1 in The Radiologic Clinics of North America, pp. 115–66. W.B.Saunders Co, Philadelphia, PA, January 1995.

[Ort96] H.V. Ortega. "Computer Simulation Helps Predict Cerebral Aneurysms." Currently available at *http://www.fluent.com/ applicat/artcl/aneur.htm*, 1996.

[Osb80] A.G. Osborn. *Introduction to Cerebral Angiography*. Harper & Row, New York, 1980.

[Pat90] S.V. Patankar. *Numerical Heat Transfer and Fluid Flow*. Hemisphere Publishing Corporation, Washington, 1990.

[Ped95] T.J. Pedley. "High Reynolds number flow in tubes of complex geometry with application to wall shear stress in arteries." *Biological fluid dynamics:symposia of the Society for Experimental Biology*, **49**:229–41, 1995.

[PFH88] K. Perktold, H. Florian, D. Hilbert, and R. Peter. "Wall shear stress distribution in the human carotid siphon during pulsatile flow." *Journal of Biomechanics*, **21**:663–71, 1988.

[PHS93] E.J. Potchen, E.M. Haacke, J.E. Siebert, and A. Gottshalk. *Magnetic Resonance Angiography: Concepts and Applications*. Mosby, St.Louis, 1993.

[PKH88] K. Perktold, T. Kenner, D. Hilbert, B. Spork, and H. Florian. "Numerical blood flow analysis: arterial bifurcation with a saccular aneurysm." *Basic Research in Cardiology*, **83**:24–31, 1988.

[PLZ79] H.W. Pia, C. Langmaid, and J. Zierski. *Cerebral Aneurysms: Advances in Diagnosis and Therapy*. Springer-Verlag, Berlin, 1979.

[PPR89] K. Perktold, R. Peter, and M. Resch. "Pulsatile non-Newtonian blood flow simulation through a bifurcation with an aneurysm." *Biorheology*, **26**:1011–30, 1989.

[Ram87] R.G. Ramsey. *Neuroradiology*. W.B. Saunders Company, Philadelphia, 1987.

[RDS95] G. Rubin, M. Dake, and C. Semba. "Current status of three–dimensional spiral CT scanning for imaging the vasculature." In J. Yao and W. Pearce, editors, *Vascular Imaging.*, number 33:1 in The Radiologic Clinics of North America, pp. 51–70. W.B.Saunders Co, Philadelphia, PA, January 1995.

[Rey83] O. Reynolds. "An experimental investigation of the circumstances which determine whether the motion of water shall be direct or sinous and of the law of resistance in parallel channels." *Philosophical Transactions of the Royal Society of London*, **174**:935–87, 1883.

[Rus95] J.C. Russ. *The Image Processing Handbook*. CRC Press, Boca Raton, 1995.

[Sch88] H.R.. Schwarz. *Finite Element Methods.* Academic Press, New York, 1988.

[See94] E. Seeram. *Computed Tomography.* J.A.Majors Company, New York, 1994.

[SGR92] C.M. Strother, V.B. Graves, and A. Rappe. "Aneurysm hemodynamics: an experimental study." *American Journal of Neuroradiology*, **13**:1089–95, 1992.

[SHC89] A.M. Seifalian, D.J. Hawkes, A.C. Colchester, and K.E. Hobbs. "A new algorithm for deriving pulsatile blood flow waveforms tested using stimulated dynamic angiographic data." *Neuroradiology*, **31**:263–9, 1989.

[SHH91] A.M. Seifalian, D.J. Hawkes, C.R. Hardingham, A.C. Colchester, and J.F. Reidy. "Validation of a quantitative radiographic technique to estimate pulsatile blood flow waveforms using digital subtraction angiographic data." *Journal of Biomedical Engineering*, **13**:225–33, 1991.

[SML96] W. Schroeder, K. Martin, and W Lorensen. *The Visualization Toolkit.* Prentice Hall, Norwalk, CT, 1996.

[Son97] Nicki P. Sonpar. *"Constructing Surface Models of Complex Vascular Malformations from Cross-Sectional Angiography Data."*. Master's thesis, University of California, Los Angeles, Computer Science Department, 1997.

[SPB92] T. Schrader, R.A. Peattle, E.I. Bluth, and C.E. Comstock. "A qualitative investigation of turbulence in flow through a model abdominal aortic aneurysm." *Investigative Radiology*, **27**:515–9, 1992.

[SPL87] H.J. Steiger, A. Poll, D.W. Liepsch, and H.J. Reulen. "Basic flow structure in saccular aneurysms: a flow visualization study." *Heart and Vessels*, **3**:55–56, 1987.

[Spr93] P. Sprawls Jr. *Physical Principles of Medical Imaging.* Aspen Publishers Inc., Gaithesburg, 1993.

[SSW88] P.K. Sahoo, S. Soltani, A.K.C. Wong, and Y.C. Chen. "A survey of thresholding techniques." *Computer Vision, Graphics, and Image Processing*, **41**:233–60, 1988.

[Ste95] T.L. Stedman. *Stedman's Medical Dictionary, Illustrated.* Williams & Wilkins, New York, 1995.

[SUS94] N. Sugimoto, C. Uyama, T. Sugahara, and Y. Yanagihara. "Estimation of 2–D blood flow velocity map from cine-angiograms: algorithm using overlapping block set and illustration of vortex flow in abdominal aneurysm." *Medical and Biological Engineering and Computing*, **32**:178–84, 1994.

[Sys97] GE Medical Systems. "GE Research Workstation." Currently available at *http://www.crd.ge.com/rws*, 1997.

[SYU89] N. Sugimoto, Y. Yanagihara, C. Uyama, and T. Sugahara. "A study of blood flow analysis on cineangiogram applying optical flow method[In Japanese]." *IEICE Technical Report MBE89-121*, **89**:59–66, 1989.

[TNY92] W. Taki, S. Nishi, K. Yamashita, A. Sadatoh, I. Nakahara, H. Kikuchi, and H. Iwata. "Selection and combination of various endovascular techniques in the treatment of giant aneurysms." *Journal of Neurosurgery*, **77**:37–42, 1992.

[TY94] T.W. Taylor and T. Yamaguchi. "Three-dimensional simulation of blood flow in an abdominal aortic aneurysm: Steady and unsteady flow cases." *Journal of Biomechanical Engineering*, **116**:89–97, 1994.

[Udu94] J.K. Udupa. "Multidimensional Digital Boundaries." *Graphical Models and Image Processing*, **56**:311–23, 1994.

[Udu96] J.K. Udupa. *The 3DVIEWNIX Software System Version 1.1. User Manual.* Medical Image Processing Group, Department of Radiology, University of Pennsylvania, Philadelphia, PA, 1996.

[VD94] L. Vincent and E.R. Dougherty. "Morphological segmentation for textures and particles." In E.R. Dougherty, editor, *Digital Image Processing Methods*, chapter 2, pp. 41–102. Marcel Dekker,Inc., New York, 1994.

[Whi74] F.M. White. *Viscous Fluid Flow.* McGraw-Hill Book Company, New York, 1974.

[Whi91] F.M. White. *Viscous Fluid Flow.* McGraw-Hill Book Company, New York, 1991.

[WNM94] N.P. Weatherill, O. Nassan, D.L. Marcum, and M.J. Marchant. "Grid generation by the Delaunay triangulation." In N.P. Weatherhill, editor, *Grid Generation. Lecture series 1994-02*, chapter 1, pp. 1–118. von Karman Institute for Fluid Dynamics, Rhode Saint Genese, 1994.

[YK94] K. Yucel and J. Kaufman. "Magnetic Resonance Imaging and Magnetic Resonance Angiography of Aortic Aneurysms." In J. Yao and W. Pearce, editors, *Aneurysms. New findings and treatments*, chapter 12, pp. 133–43. Prentice Hall, Norwalk, CT, 1994.

[Zie62] K.L. Zierler. "Theoretical basis of indicator-dilution for measuring flow and volume." *Circulation Research*, **10**:393–407, 1962.